Unterschrift (Betreuer)

TECHNISCHE UNIVERSITÄT WIEN

Diplomarbeit

Laser-sub-cycle Fragmentation Dynamics of Argon Dimers

Ausgeführt am Institut für Photonik
der Technischen Universität Wien

unter der Leitung von
Univ.Prof. PhD Andrius Baltuska
und
Senior Scientist Dipl.-Ing. Dr.techn. Markus Kitzler

durch
Vimal Kunnummel BSc

Wien, 05.04.2016

Unterschrift (Student)

Thanks to ...

Prof. Andrius Baltuska for giving me the opportunity to work on this interesting topic and granting me a stipend so that I could fully concentrate on the work. I would like to thank especially Dr. Markus Kitzler as my direct supervisor for the excellent support during the whole year. Furthermore, I would like to thank Sonia Erattupuzha for sharing her expertise in the laser lab and for all the discussions dealing with the research. Thanks also to Dr. Ondrej Hort, with whom I had the pleasure to work on high harmonics and attosecond pulse generation schemes and to Seyedreza Larimian, Dr. Xinhua Xie and Vaclav Hanus for their help with the data analysis. I would also like to thank all other members of the Ultrafast Laser Group. Thanks also to all my friends but especially my Physics colleagues Martin, Marco, Sebastian and Stefan without whom my studies would never have been that much fun. Special thanks to my to-be wife Olivia for always standing by my side and being patient with me. Thanks also to my (future) parents-in-law for the support and encouragement. I am also very very thankful to my parents and my sister for always having faith in my capabilities and very grateful for supporting me throughout my whole life.

Contents

1 Introduction

This work is the result of my research conducted together with the scientists of the Ultrafast Laser Group at TU Vienna. I had the opportunity to work with a state-of-art Titanium sapphire femtosecond laser system and gain hands-on experience operating the complex laser system. Furthermore, I had the chance to get acquainted with the COLTRIMS experimental setup, both in the preparation of the gas jet and the laser beam optimization but also in the data acquisition process, by working together with my supervisors Dr. Markus Kitzler and Sonia Erattupuzha. The objective of the research was to study the newly reported electron trapping mechanism termed frustrated tunneling ionization. Using femtosecond laser pulses delivered by a Ti:sa laser system, argon dimers were ionized and their subsequent fragmentation studied using the COLTRIMS technique. My main role was to process the accumulated data and gain insight into the fragmentation mechanisms. This was done by conducting a literature survey to get an overview of the current research status and the theoretical developments. In a next step the acquired data was analyzed to gain insight into the physical processes which lead to these interesting electron recapture mechanisms. Apart from working on this topic, I had the chance to work simultaneously on high harmonics and attosecond pulse generation methods which was very useful to gain a broader understanding of the principles of ultrashort pulse generation, characterization and applications in various areas.

The goals of this work are to obtain insight into laser-driven electron recapture processes on laser-sub-cycle time-scales. These electron recapture processes in strong laser fields, also known as frustrated tunneling ionization [10], have been the subject of a number of studies [10-14]. However, the mechanisms leading to this process are still not completely understood. Additionally, all studies so far used pulses consisting of many laser cycles with pulse durations varying from 25 to 35 fs. However, since it has been shown that the recapturing process can be explained in the context of electron rescattering [10-14], it should be sensitive to the sub-cycle evolution of the laser electric

field and consequently depend on the carrier envelope phase (CEP) for few-cycle pulses. Using the laser field as a sub-cycle temporal reference should therefore allow obtaining insight into the trapping dynamics.

Rare gas dimers are ideal objects to study the recapturing dynamics as they essentially resemble two separate atoms due to the large internuclear distance but at the same time allow detecting the highly excited ions unambiguously by exploiting momentum conservation between the two Coulomb exploding argon ions [12-14]. From a phenomenological point of view electron trapping (or recapturing) processes are well-established members of the family of typical strong-field driven processes such as rescattering double ionization, rescattering excitation, above threshold ionization or high harmonic generation. Hence, the study of the electron trapping dynamics add to a more complete understanding of the interaction of strong laser fields with atoms or molecules. The results show that the measurements with few-cycle pulses reproduce the results obtained earlier with longer pulses [12-14], highlighting the field-driven character of the involved processes. Furthermore, the electron emission and recapturing dynamics shows a very pronounced dependence on the CEP of few-cycle laser pulses. In accordance with the proposed theory [10-14], it was found that the CEP dependence of the FTI peaks also closely resemble those of the Coulomb explosion peak of the higher charged dimer ion.

2 Theoretical Aspects

Laser-Matter interaction cannot be studied without foundations of quantum mechanics as most phenomena cannot be explained in terms of classical physics. Indeed the laser itself is a result of the quantification of energy leading to discrete energy levels in the "microscopic" quantum world. This contradicts the classical view where the energy range of the particles is continuous. Many phenomena arising in the quantum world are counterintuitive and more importantly the equations describing them are very difficult to solve. The famous Schrödinger equation, Eq. (2.1),

$$\left\{-\frac{\hbar^2}{2m}\nabla^2 + V(\mathbf{r},t)\right\}\psi(\mathbf{r},t) = i\hbar\frac{\partial}{\partial t}\psi(\mathbf{r},t) \tag{2.1}$$

where $V(\mathbf{r},t)$ is a time dependent potential, and $\psi(\mathbf{r},t)$ the wave function, can only be analytically solved for simple systems and solving the equation with three (or more) interacting quantum particles is very hard, if not impossible with available computational tools. As a result, sensible approximations must be made to model a specific problem. In many cases it is sufficient to use a hybrid quantum mechanical - classical picture, which is also used to solve many laser-matter interaction problems. In the following section, basic theoretical background needed to understand the ionization mechanisms induced in the atoms and molecules with ultrashort laser pulses, will be provided.

It should be noted that atomic units (a.u.) are used in this work unless explicitly denoted otherwise. Hereby, following fundamental physical constants are set to unity: electron mass m_e, elementary charge e, reduced Planck's constant $\hbar$ and Coulomb's constant $k_e = 1/(4\pi\epsilon_0)$.

2.1 Laser

The laser is an unique light source of modern physics which became indispensable in the recent years. Lasers deliver spatially coherent light beams which can be focused very tightly. Furthermore, in short-pulse lasers, due to temporal coherence, it is possible to generate light bursts that have a duration of only few optical cycles and, therefore,

achieve very high peak powers. As a consequence of the spatial and temporal coherence, electric field strengths exceeding the binding potential of an atom can be reached in focused laser beams even from small tabletop short-pulse laser systems. The laser consists mainly of three components: an active medium, in which an excited state is artificially populated due to external energy supply; an energy pump, which leads to the population inversion and an optical resonator, which stores the emitted radiation from the active medium, so that the induced emission becomes much more probable than the spontaneous emission. The resulting radiation can then be out coupled at the ends of the resonator.

The main methods to generate pulsed laser light are gain switching, Q-switching and mode-locking. Mode-locking is used to generate pulsed laser light with very short pulse durations while the delivered power is not as high as Q-switching which delivers high power in the nanosecond pulse duration range. In principle mode-locking is achieved by inducing a fixed phase relationship between the longitudinal modes in the resonator. Due to the Fourier relationship between frequency and time $\triangle E \triangle t \geq \frac{\hbar}{2}$, a broad spectrum is furthermore needed to achieve short pulse durations.

Today, mode locked solid state lasers like Titanium-doped sapphire lasers are commonly used to generate femtosecond pulses because of practical advantages such as simplicity, compactness, reproducible performance, reliability and a long life time of solid state laser systems compared to dye lasers which were initially used [2]. A crystal of sapphire (Al_2O_3) doped with Titanium ions is used as the laser medium [3]. Ti:sa lasers are tunable lasers which emit light in a wide range from 650 to 1100 nanometers, making them very useful for scientific research. They are usually pumped with another laser with a wavelength of 514 to 532 nm like for example argon-ion lasers (514.5 nm), frequency doubled Nd:YAG, Nd:YLF or Nd:YVO lasers (527-532 nm) and more recently with GaN laser diodes.

2.2 The Three Step Model

The three step model or the simple man's model is used to to describe strong-field

induced ionization dynamics in atoms and molecules in a classical picture [7]. Mechanisms leading to high harmonic generation for example can be qualitatively explained in this model. In this picture the strong-field of the laser pulse distorts the atomic potential in such a way that the electron can be tunnel ionized into the continuum where it is further accelerated in the oscillating field of the laser pulse. In fact, the classical Newton equations used in this model show that electrons leaving the ion core at certain trajectory angles are redirected back towards the core by the oscillating field. The electron that has picked up energy from the electromagnetic field of the driving laser pulse can induce several processes. It can scatter elastically leading to diffraction, inelastically which could lead to excitation or to ionization of the parent ion or generate high harmonics by recombining with the parent ion. The model predicts that the maximum energy gained by the electron in the oscillating field is 3.17 U_p, where $U_p = \frac{E_0^2}{4\omega^2}$ is the ponderomotive energy, E_0 the amplitude of the electric field and ω the laser carrier frequency.

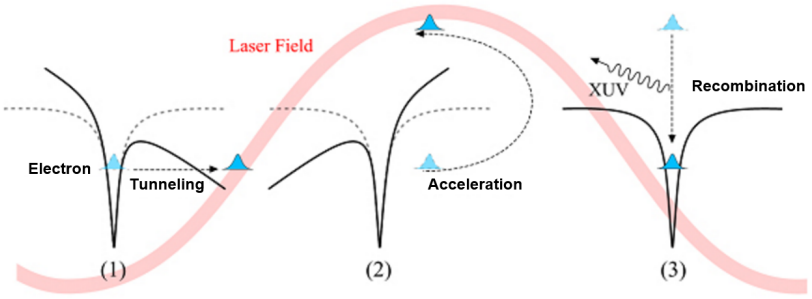

Fig. 2.1. The three step model or simple man's model of high harmonic generation. The electron is tunnel ionized in the first step (1) and accelerated in the laser field and redirected to the parent ion in a second step (2) and recombines with the atom to generate high harmonics (3) in the last step. Adapted from [8].

It should be noted that the Coulomb attraction of the parent ion is neglected in this model (strong field approximation). A plausible reason for this approximation is that the effect of ponderomotive acceleration is significantly stronger than that exerted by the Coulomb force. This leads to the question if there are also processes where the

Coulomb potential cannot be neglected in case the energy the electron gains from the laser field is not very high. It turns out that this case is applicable to the process termed frustrated tunneling ionization which will be studied in this work.

2.3 Laser-induced Ionization Processes

Ionization is described as the process where one or more electrons are removed from atoms or molecules due to some kind of external supply of energy (via electrons, photons or ions) which exceeds the ionization potential of the atom or molecule. Atoms and molecules can be easily ionized by using laser light as that external energy supply. Ionization can further induce fragmentation processes in molecules as a result of the subsequent Coulomb repulsion of the constituents. This process is called Coulomb explosion. Depending on the number of the removed electrons, one differentiates between single, double or higher ionization processes. Higher ionization may result from sequential as well as non-sequential processes. In sequential ionization processes, the electrons are removed independently of each other due to the external laser field. Therefore sequential ionization can be seen as a sequence of one electron ionizations where the ionization potential for each electron only depends on the charge state of the ion. Conversely, in non-sequential processes, already ionized electrons are involved in the subsequent ionization processes. Hereby the electron is not immediately sent into the continuum after ionization and can instead be accelerated by the laser field and in many cases even driven back to the parent ion.

In intense laser fields with high peak intensities nonlinear ionization processes arise, where an ensemble of photons induces ionization of an atom. This leads to interesting phenomena like multiphoton ionization and above threshold ionization processes where more than one photon deliver the energy to ionize an atom. If N photons with the energies $\hbar\nu$ are absorbed, an electron can be ionized when

$$N\hbar\nu > E_B, \tag{2.2}$$

where E_B is the binding energy of the electron. The probability for these nonlinear processes decreases significantly with increasing number of involved photons. Nevertheless, such processes are observed in intense fields of pulsed lasers. At very high laser intensities, strong fields can furthermore distort the atomic potential in a way that the electrons can tunnel out. These phenomena are called tunnel ionization and over-the-barrier ionization. The atomic potential and the laser field create an effective potential which corresponds to a time-dependent barrier through which the electrons can tunnel. The ionization rate W of the tunneling ionization increases exponentially with the electric field strength E,

$$W \propto \exp\left(-\frac{2(2I_p)^{3/2}}{3E}\right) \tag{2.3}$$

where I_p is the ionization potential.

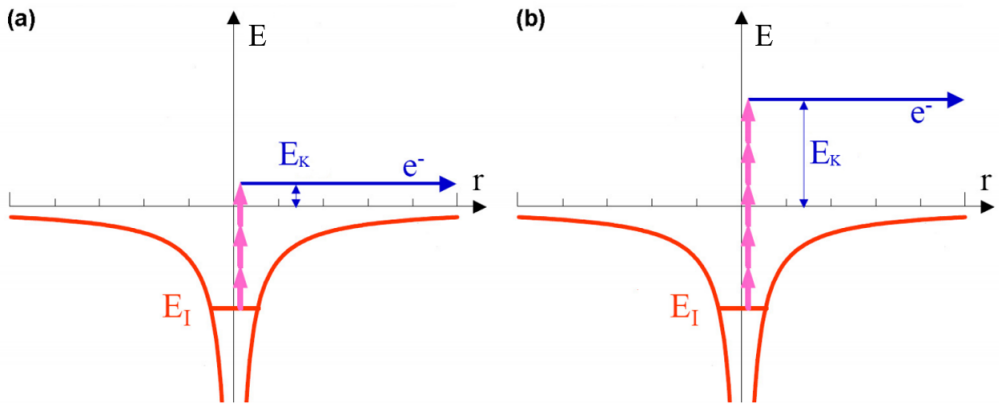

Fig. 2.2. Schematic of multi-photon ionization (a) and above-threshold ionization (b). E_I is the ionization potential and E_K the kinetic energy of the ionized electron. Adapted from [9].

The so called Keldysh parameter $\gamma = \sqrt{\frac{I_P}{2U_P}} = \frac{\omega}{\varepsilon_0}\sqrt{2I_p}$ where I_p is the ionization potential, U_p the ponderomotive energy and ω the laser carrier frequency, is used to categorize the different processes. The tunneling regime is given by$\gamma \ll 1$, the multiphoton regime $\gamma \gg 1$ and the intermediate regime by $\gamma \sim 1$.

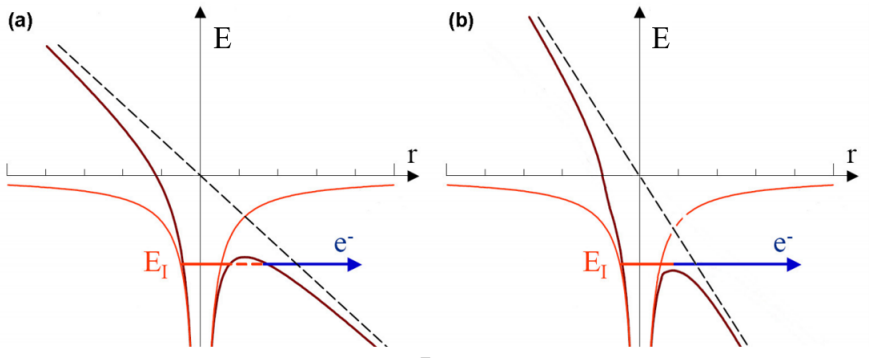

Fig. 2.3. Schematic of tunnel ionization (a) and over-the-barrier ionization (b). E_I is the ionization potential. Adapted from [9].

In the tunneling regime it is not possible to work with the models based on perturbative theory to describe the ionization processes and therefore non-perturbative models like the strong field approximation are needed.

Strong Field Approximation

The approximation made in the strong field approximation (SFA) is that the effect of the core potential is small compared to the laser field and thus can be neglected when studying the dynamics of the electron after ionization. The SFA can be used to model many strong field phenomena and is computationally much less demanding than solving the time-dependent Schrödinger equation numerically. In the simplest case, the strong field approximation is used in the single active electron picture where it is assumed that only one electron (the most weakly bound one) interacts with the laser field.

As shown in [27], the Schrödinger Equation in the length gauge of an atom under the influence of a intense laser field $E(t)$ can be written as,

$$i\frac{\partial}{\partial t}\left|\psi(r,t)\right\rangle = \left(-\frac{1}{2}\nabla^2 + V(r) + r\cdot E(t)\right)\left|\psi(r,t)\right\rangle \tag{2.4}$$

where $V(r)$ is the atomic potential. The total Hamiltonian can be split into a time-dependent part $H(t) = r\cdot E(t)$ which is determined by the laser field and a time inde-

pendent part $H_0 = -\frac{1}{2}\nabla^2 + V(r)$, therefore giving

$$H_{tot}(t) = H_0 + H(t). \tag{2.5}$$

The solution of Eq. 2.4 can be given as

$$|\psi(r)\rangle = \exp\left(-i\int_{t_0}^{t} H_{tot}(\tau)d\tau\right)|\phi_i\rangle \tag{2.6}$$

where $|\phi_i\rangle$ is the initial state at t_0. The transition probability from the initial state $|\phi_i\rangle$ to the final state $|\phi_f\rangle$ at t_f can be given as,

$$P_{if}(t_f) = -i\int_{t_0}^{t_f}\left\langle \phi_f \left| e^{-i\int_{\tau}^{t_f} H_{tot}(\tau')d\tau'} V(\tau) e^{-iH_0(\tau-t_0)} \right| \phi_0 \right\rangle d\tau. \tag{2.7}$$

The system evolves before the ionization at the point of time τ without the influence of the field, therefore only depending on H_0 and after the ionization under the influence of the laser field therefore depending on $H(t)$. For processes in strong laser fields the approximation can be made that after the ionization the Coulomb potential has negligible influence on the dynamics of the electron therefore the Hamiltonian can be written as, $H_{tot}(\tau') = H(\tau')$ which allows us to approximate the term $e^{-i\int_{\tau}^{t_f} H_{tot}(\tau')d\tau'}$ with the so called Volkov states, which describe the propagation of electrons in laser fields. Therefore the probability to measure an electron with momentum p in the final state $|\phi_f\rangle$ can be given as,

$$P_p(t_f) = -i\int_{t_0}^{t_f} e^{-i\left(\int_{\tau}^{t_f} E(\tau')d\tau' - I_p(\tau)\right)} \langle p(\tau)|V(\tau)|\phi_0\rangle d\tau. \tag{2.8}$$

where I_p is the ionization potential. Eq. 2.8 describes an electron which is ionized at τ from the initial state to the continuum and propagates afterwards under the influence of the laser field without any subsequent interactions with the atomic potential.

3 Frustrated Tunneling Ionization (FTI)

One of the main objectives of this work is to study a recently reported phenomenon termed frustrated tunneling ionization. It describes the recapture process of electrons which have initially been tunnel ionized due to the interaction with the strong laser field but are eventually trapped in high lying Rydberg states as a result of the Coulomb attraction of the parent ion. Thus, this mechanism is described in the context of a tunneling and rescattering picture. To examine the proposed model, the dependence of frustrated tunneling ionization on the carrier envelope phase offset of the laser pulse is studied in this work. In case the FTI process results from a rescattering process, a clear dependence of this process on the carrier envelope phase of the laser pulse can be expected. Furthermore, in our experiments extremely short laser pulses of 5 fs temporal duration (FWHM) are used.

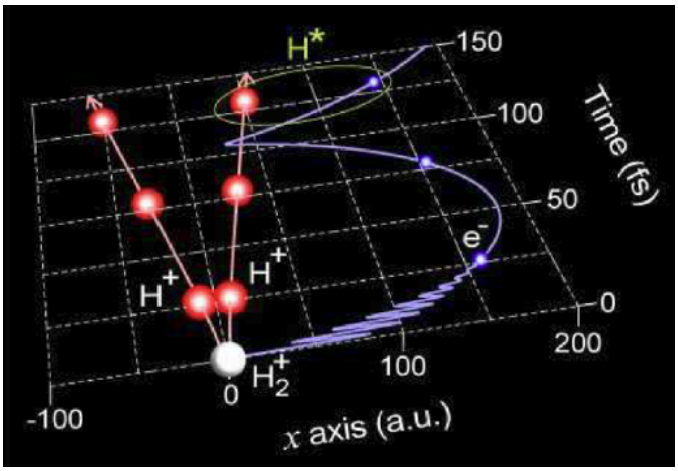

Fig. 3.1. The recapture process of a tunneled electron by one of the hydrogen ions is visualized. Due to the electron recapture into a Rydberg state a highly excited H* atom is formed [11].

This work reports the first known study of FTI with laser pulses that carry only a couple of electric field oscillations. Previous studies were performed in the multicycle regime using 25 fs or longer laser pulses. Among other advantages, the use of 5-fs pulses in this work makes it possible to investigate the carrier envelope phase (CEP) effect in frustrated tunneling ionization. The fragmentation processes are studied using the so

called Cold Target Recoil Ion Momentum Spectroscopy (COLTRIMS) technique which will be described in section 4.3. Using this experimental setup it is possible to measure the momenta of the fragmented particles and to calculate the Kinetic Energy Release (KER) which is the energy released during the dissociation process due to the Coulomb repulsion between the ionized atoms. Before the obtained results are presented, an overview of the current research status starting with the first paper reporting on this process to the latest developments, is provided in this section. The main statements of the FTI theory are the following [10-14]:

- FTI is described as a rescattering process where the tunneled electron is recaptured by its parent ion due to its attractive Coulomb field.
- Electrons which are ionized in a small window around the laser field maximum seem more likely to be recaptured as they do not gain enough drift energy from the field and are eventually left in the vicinity of the ion after the laser pulse is gone.
- Electron which are ionized from argon dimers which were oriented perpendicular to the laser polarization direction at the instant of ionization are more likely to be recaptured.
- The "diameter" of the Rydberg orbital is much larger than the internuclear distance of argon dimers and therefore, when the tunneled electron is recaptured, it is not clear on which ion the electron localizes. Only when the internuclear distance of the two ions due to their Coulomb repulsion reaches the order of the Rydberg orbital diameter does the electron start to screen the charge of one of the two ions.
- The tunneled electron tends to localize on the ion with the higher charge state.
- Multiple electron recapture is possible.

3.1 Frustrated Tunneling Ionization in He Atoms

In the paper [10], Nubbemeyer et al. measured for the first time excited neutral He atoms (He*) surviving strong laser fields. The existence of these neutral atoms was shown for different laser intensities. They named this neutral exit channel "frustrated tunneling ionization". The explanation they delivered to this process is as follows: the laser induced tunneling electron does not gain enough drift energy from the laser pulse and therefore becomes recaptured due to the Coulomb potential of the parent ion. So this process can be integrated to the wide range of phenomena explained in the tunneling-rescattering model. They furthermore measured that the yield of these neutral atoms surviving the strong laser field rapidly sank when the laser polarization was slowly changed from linearly polarized to circularly polarized further supporting this explanation as rescattering is completely suppressed in the case of circularly polarized laser light. In the case of circularly polarized light, the final drift energy is independent from when the ionization takes place within the sub-cycle and is always large ($E_{drift} = E^2/2\omega^2$, where E is the electric-field strength of the laser pulse and ω the laser frequency).

3.2 Ionization Mechanisms in H_2 Molecule

In 2009, it was shown that this phenomenon of FTI also exists in molecules [11]. Excited neutral H atoms (H*) surviving the process after interaction of H_2 molecules with an intense laser fields was observed.

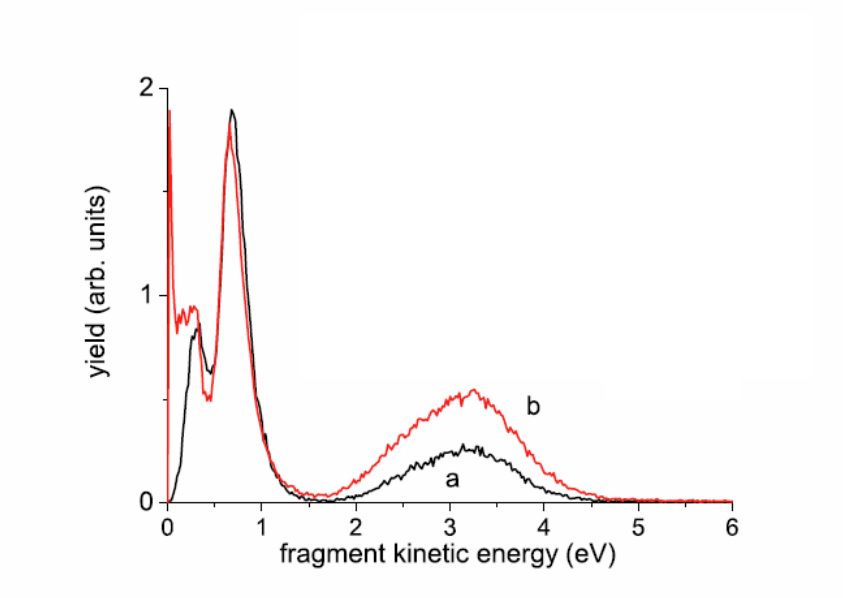

Fig. 3.2. The kinetic energy release spectrum of the fragments (a) H^+ (black curve) and (b) H* (red curve) after strong field ionization are shown [11].

Fig. 3.2 already shows one of the characteristics of the FTI mechanism. It can be seen in Fig. 3.2 that the KER spectrum of the H* neutral atoms is very similar to that of the H^+ ions. The highest peak in Fig. 3.2 in case of the H^+ ion stems from the Coulomb explosion of the H_2^{2+} molecule after sequential double ionization which means that it is a correlated process. Because the spectrum of H* is similar to that of H^+, the high KER peak in this case should also stem from a correlated process, therefore a partner H* or H^+ must exist.

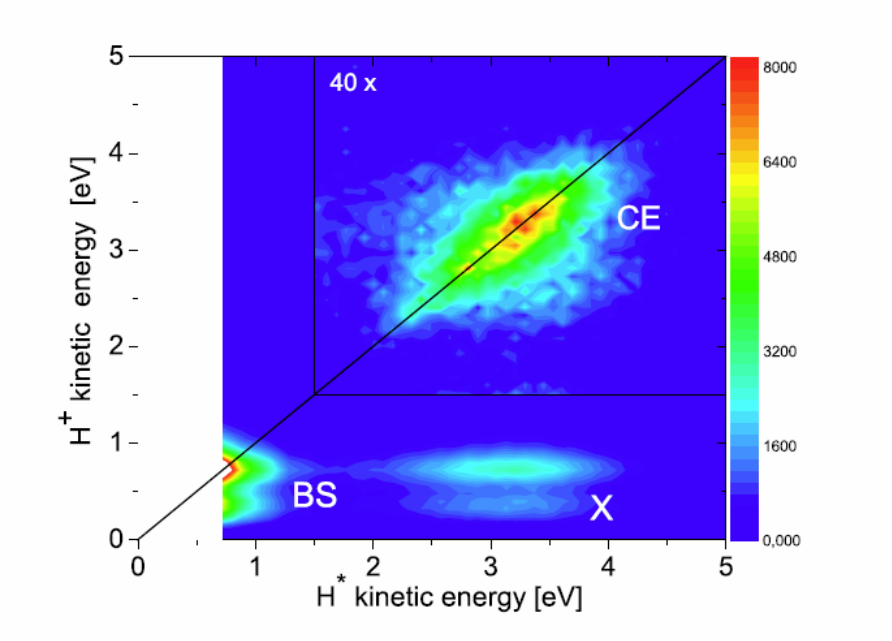

Fig. 3.3. The time of flight (ToF) of the excited neutral hydrogen atom H* is plotted versus the time of flight of the hydrogen ion H^+. Events which are found on the black line correspond to correlated events [11].

As can be seen in Fig. 3.3, there is a clear correlation between the H* and H^+ ions. This indicates that the assumptions made to describe this process are valid. The H* neutral atoms emerge after the interaction because in that case the second tunneled electron gets recaptured by the parent ion. The main difference between the molecular and atomic case that the in this molecular case there are two H^+ ions which could recapture the second tunneled ion.

3.3 Ionization Mechanisms in Argon Dimer

More groups [12,13] looked at a more complicated molecule to study the FTI process. They chose the noble gas dimer argon because it can be used as a model for two connected atoms due to its structure. The argon dimer has a rather large equilibrium internuclear distance and therefore the atomic orbitals are strongly localized on the atoms but they are still bound due to Van der Waals forces. In [12] the double ionization process of the argon dimer in a strong field and its fragmentation was studied. Apart

from the expected Coulomb explosion the group measured higher kinetic energy release peaks and the highest measured peak was identified as the result of the FTI process. As can be seen in Fig. 3.4, the KER distribution for linearly polarized light shows three peaks denoted as a, b and c, with a dominant peak at 3,8 and two further peaks at 5.3 and the highest KER peak at 7.3 eV which disappears for circularly polarized light. The mechanisms leading to the three distinct peaks a, b, c will be explained in detail in the following sections.

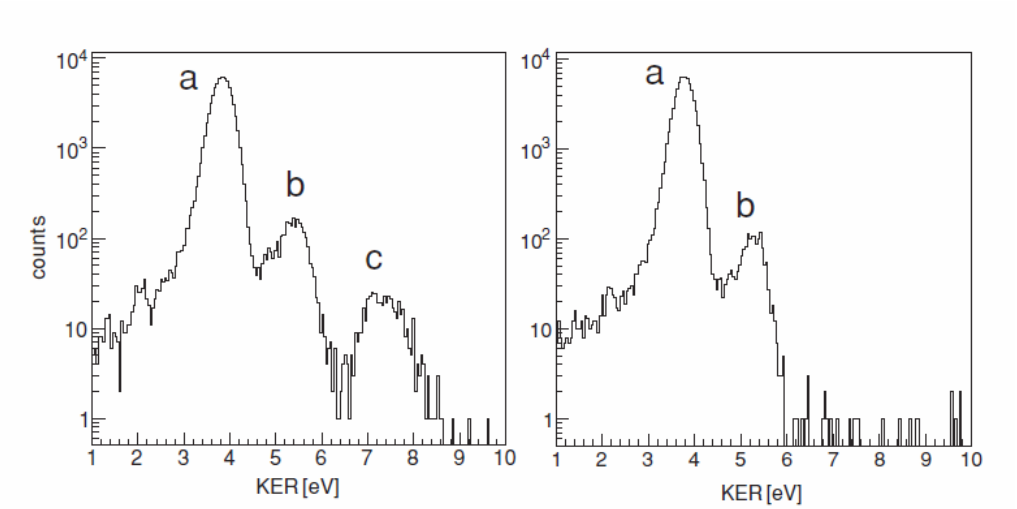

Fig. 3.4. Kinetic energy release spectrum of Ar^+ ions for linearly polarized (left panel) and for circularly polarized light (right panel). Notably the high energy peak at 7.2 eV vanishes for circularly polarized light [13].

Peak A

This is the KER peak which stems from the Coulomb explosion of a doubly-ionized argon dimer. In a first step an electron from the $3p$ shell of each atom is sequentially removed. Due to Coulomb repulsion the argon dimer explodes leading to this KER peak. One can calculate the equilibrium distance when the Coulomb explosion took place which is in this case 3.9 Å, a value close to the equilibrium distance for argon dimers.

Role of argon dimer geometry

As can be seen in Fig. 3.5. the double ionization (DI) probability of argon dimers which are lying perpendicular to the laser beam polarization is much lower than those which are lying parallel to the laser beam polarization. As the pulse duration used in this experiment is very short, no active alignment due to the laser pulse can be expected. This proves that there is a dependence of double ionization on the geometry of the argon dimer [12].

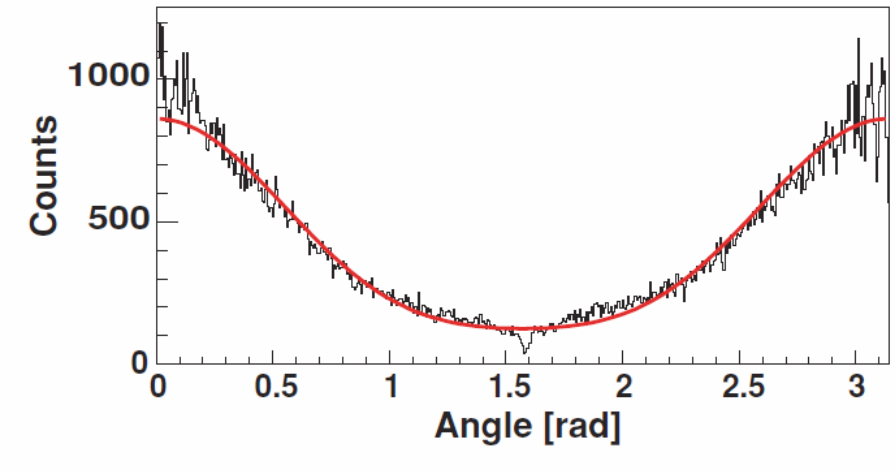

Fig. 3.5. For the Coulomb explosion peak denoted (a) in Fig. 3.4, the angular distribution of the fragments is shown. Plotted is the number of events per solid angle element $d\Omega = 2\pi \cos\theta d\theta$ as a function of θ, the angle between the laser beam polarization axis and the direction of emission of one of the Ar^+ ions [12].

Peak B

This peak does not originate from the FTI process but two different possibilities for its explanation have been proposed:

1. Laser induced charge transfer followed by radiative reverse charge transfer
2. Two center ionization to a highly excited state

The first mechanism can be explained in the following way: the starting point is the two-site double ionization of the dimer similar to the mechanism responsible for peak (a) after which a laser-induced charge transfer from one ion to the other one takes place. This results in a one-site doubly-ionized configuration Ar^{2+}-Ar molecule, where the Ar atom is in the electronic ground state. Afterwards, due to a charge-induced dipole interaction the Ar^{2+}-Ar the internuclear bond length between the two constituents decreases. It is possible that from this configuration a process termed radiative charger transfer (RCT) takes place. Hereby one photon is emitted and the the dimer decays to a two-site ionized configuration Ar^{+}-Ar^{+}. The probability for this process increases exponentially with decreasing R. The higher KER stems therefore from the smaller internuclear distance on the instant of explosion in this case.

In the second case the higher KER can be explained by a very steep, $> 1/R$, curve of the dissociation potential. Inelastic collision of the electron with other atoms could explain the energy gain. The dissociation itself originates from equilibrium distance.

Peak C

The most interesting peak is the one with the highest KER which is denoted as peak (c) which is a result of the frustrated tunneling ionization mechanism where three electrons are involved.

Frustrated triple ionization

In order to get trapped into a high lying Rydberg state the final drift energy of the electron has to be small which is true for electrons ionized close to the maximum of the electric field of the pulse. The process which leads to this high KER peak can be explained as follows: The first step which is similar to the two-site tunnel ionization for peak is followed by the tunnel ionization of a third electron which then would be trapped upon recollision into a Rydberg state [12,13].

The important difference compared to the case where only two electrons are involved is that the third electron is now trapped into a Rydberg state with an orbit radius much

larger than the equilibrium distance between the two ions. Therefore, the electron will not be localized in this stage on any of the two ions meaning that the two ion dissociate initially on a $2/R$ potential after they feel the Coulomb repulsion of each other. Only when the internuclear distance between the two ions reaches close to the radius of the Rydberg orbit will the electron spontaneously localize on one of the nuclei. The results show that the electron predominantly localized on the Ar^{2+} ion. After the electron localization the dissociation continues on a $1/R$ potential.

3.3.1 Multiple Electron Recapture Mechanisms

It was shown in [14] that for high intensity pulses (8×10^{14} W/cm^2) it is possible to produce multiply charged Argon dimer ions which can be denoted as (Ar^{p+}, Ar^{q+}) where ($p + q = Q$, the total ion charge). This leads to a situation when more than one tunneled electron can be trapped during the FTI process into the Rydberg states. Furthermore it should be clarified which of the two parent ions recaptures predominantly the rescattered electrons.

After the ionization of the electrons and the subsequent trapping the dissociation is in a first step driven by the ions with the charges p and q which are not screened by the the recaptured electrons in much bigger orbits compared to the bond length between the two ions. Only when the system reaches the size of the orbit radius of the trapped electron will the electrons localize at the ions and start screening the charges and as a result forming the final ionic states of Ar^{n+}, Ar^{m+} with the coincidentally detectable charges (n, m).

The following fragmentation channels were considered in [14]:

$$Ar_2^{2+} \rightarrow Ar^+ + Ar^+ \Longrightarrow Ar(1,1) \tag{3.1}$$

$$Ar_2^{3+} \rightarrow Ar^{2+} + Ar^+ \Longrightarrow Ar(2,1) \tag{3.2}$$

$$Ar_2^{4+} \rightarrow Ar^{2+} + Ar^{2+} \Longrightarrow Ar(2,2) \tag{3.3}$$

$$Ar_2^{4+} \rightarrow Ar^{3+} + Ar^{+} \Longrightarrow Ar(3,1) \tag{3.4}$$

$$Ar_2^{5+} \rightarrow Ar^{3+} + Ar^{2+} \Longrightarrow Ar(3,2) \tag{3.5}$$

$$Ar_2^{6+} \rightarrow Ar^{3+} + Ar^{3+} \Longrightarrow Ar(3,3) \tag{3.6}$$

$$Ar_2^{7+} \rightarrow Ar^{4+} + Ar^{4+} \Longrightarrow Ar(4,3) \tag{3.7}$$

As shown in Fig. 3.6, the largest peak in the KER spectrum of all channels is the one resulting from Coulomb explosion of the two ions. The higher peaks which only appear for linearly polarized light show that they are formed due to rescattering processes.

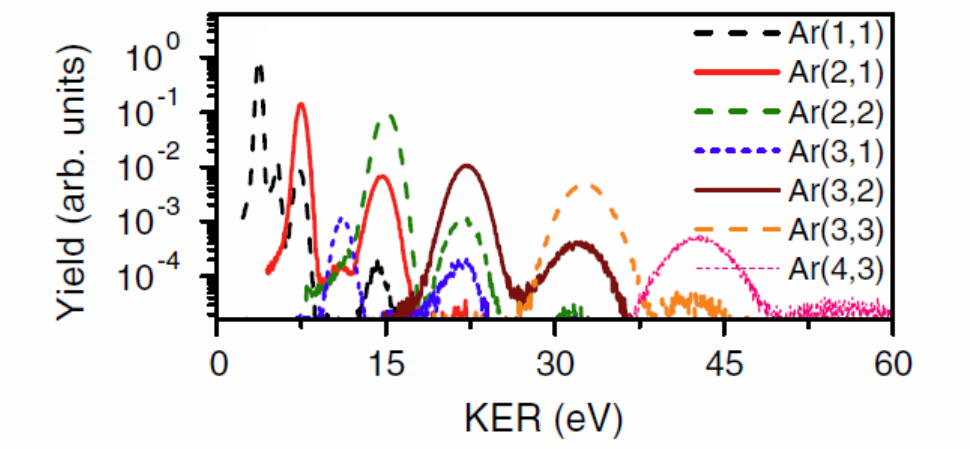

Fig. 3.6. The KER spectrum of various fragmentation channels of Ar_2 after strong field ionization [14].

The results indicate that the charge symmetric channels, which are predominantly produced when the trapped electron localizes on the ion with the higher charge, are produced with a higher probability than the charge asymmetric one. As an example starting from the initial ionic dimer Ar_2^{4+}, the production rate of Ar(2,2) is much higher than Ar(3,1). From the ionic dimer Ar_2^{6+}, only the channel Ar(3,3) was measured.

As to be expected, the higher KER peaks lie close to those of higher charge states. One can therefore conclude that, although the measurable charge states are (n, m), the KER seems to result (at least at the beginning) from the Coulomb explosion of the higher initial state (p,q). Table I shows that measured statistics of the different KER

peaks and for the peaks which result from the FTI process, the recapture probability is given.

Dissociation channels	Ratio (%)	Recapture probability (%)
Ar(1, 1): 3.8 eV	53.88	
Ar(1, 1): 5.3 eV	0.93	
Ar*(1, 1): 7.3 eV	0.95	6.02 [+ 1e from Ar(2, 1)]
Ar*(1, 1): 14.3 eV	0.03	0.13 [+ 2e from Ar(2, 2)]
Ar(2, 1): 7.5 eV	14.82	
Ar ∗ (2, 1): 10.9 eV	0.05	20.0 [+ 1e from Ar(3, 1)]
Ar*(2, 1): 14.7 eV	1.51	6.70 [+ 1e from Ar(2, 2)]
Ar*(2, 1): 21.7 eV	0.01	0.26 [+ 2e from Ar(3, 2)]
Ar(2, 2): 15.1 eV	21.00	
Ar*(2, 2):21.9 eV	0.35	9.21 [+ 1e from Ar(3, 2)]
Ar*(2, 2): 31.7 eV	0.01	0.41 [+ 2e from Ar(3, 3)]
Ar(3, 1): 11.1 eV	0.20	
Ar*(3, 1): 21.6 eV	0.06	1.58 [+ 1e from Ar(3, 2)]
Ar(3, 2): 22.2 eV	3.38	
Ar*(3, 2): 32.0 eV	0.21	8.54 [+ 1e from Ar(3, 3)]
Ar(3, 3): 32.7 eV	2.24	
Ar*(3, 3): 42.0 eV	0.02	5.88 [+ 1e from Ar(4, 3)]
Ar(4, 3): 42.8 eV	0.32	
Ar*(4, 3): 55.6 eV	0.03	— [+ 1e from Ar(4, 4)]

Table I. The yield ratio and electron trapping probability of fragmentation channels of Ar_2. The electron trapping probability is estimated by normalizing the yield of the electron trapping channel to the total yield of all the channels with the same initial charge state [14].

The results also show that two electron-recapture is possible. The highest KER peak in the Ar(1,1) channel originates from two electron recapture of the initial ion state Ar(2,2), where each ion recaptured one electron into a Rydberg state. Furthermore the peaks at 21,7 and 21,7 eV for the fragmentation channels Ar*(2,1) and Ar*(2,2) also stem from two electron-recapture from the initial states Ar(3,2) and Ar(3,3).

Dependence of the dimer orientation on recapture process

It was noticed so far that those electrons were trapped which tunneled close the the maximum of the electric-field. Additionally, results [14] show that those argon dimers which are aligned parallel to the electric field are ionized with a higher probability than those aligned perpendicular to the electric field. These argon dimers which are aligned parallel to the electric field are not ionized close the the maximum of the laser pulse field. Therefore, they subsequently accumulate enough kinetic energy to leave the Coulomb potential of the parent atom. This is not the case for argon dimers aligned perpendicular to the electric field. These electrons tunnel through the barrier during a very narrow period close the the electric field maximum. They do not acquire enough energy in the oscillating field to become fully ionized and therefore are more likely recaptured. Thus it can be concluded that the electrons involved in the FTI mechanism tunnel from dimers oriented orthogonal to the E-field of the pulse.

Estimation for the size of the Rydberg orbital

An approximation of the radius of the Rydberg electron orbital $\langle r \rangle$ is given as follows,

$$\langle r \rangle = (0.5 Q \tau^2)^{1/3} \tag{3.8}$$

where Q is the total unscreened initial charge state of the two ions and τ the pulse duration [14]. This approximation was made for pulses with a duration of 35 fs but will most probably not be valid anymore for very short pulses. The quantum number $\langle n \rangle$ which can be assigned to electrons in such high lying Rydberg states can be given as

$$\langle n \rangle = (2Q \langle r \rangle / 3)^{1/2}, \tag{3.9}$$

and the Kepler period for $\langle T_k \rangle$ for the Rydberg electrons for one full period given as

$$\langle T_k \rangle = 2\pi \langle n \rangle^3 / Q^2. \tag{3.10}$$

Localization of the electron on argon ion

The results [14] show that in case of two argon ions with different charge states, the electrons localizes on the one with the higher charge state. For example in the case of the fragmentation channel Ar(2,1), the KER peak at 10.9 eV stems from one electron-trapping of Ar(3,1) state and the peak at 14.7 eV from one electron-trapping from Ar(2,2) state. The probability to reach the Ar*(2,1) state is much higher from the Ar(3,1) state. Furthermore, the results show that the Ar*(2,2) peak is more probable than the Ar*(3,1) peak because from the initial state Ar(3,2), the trapped electron more likely is bound by the Ar^{3+} ion than the Ar^{2+} ion.

3.4 FTI Mechanism in Asymmetric Molecules

In this section, a review of the state of the art for the study of the recapture process in asymmetric molecules is presented. Specifically, focus will be on experiments on N_2Ar reported in [15]. The main motivation for this experiment is to find out which constituent recaptures the electron, the molecular N_2 or the the argon ions. Furthermore, they compare the results gained from the N_2Ar breakup with results from Ar-Ar and N_2-N_2 fragmentation channels.

Following fragmentation channels were analyzed:

$$N_2Ar^{2+} \rightarrow N_2^+ + Ar^+ \Longrightarrow N_2Ar(1,1) \tag{3.11}$$

$$N_2Ar^{3+} \rightarrow N_2^{2+} + Ar^+ \Longrightarrow N_2Ar(2,1) \tag{3.12}$$

$$N_2Ar^{3+} \rightarrow N_2^+ + Ar^{2+} \Longrightarrow N_2Ar(1,2) \tag{3.13}$$

$$N_2Ar^{4+} \rightarrow N_2^{2+} + Ar^{2+} \Longrightarrow N_2Ar(2,2) \tag{3.14}$$

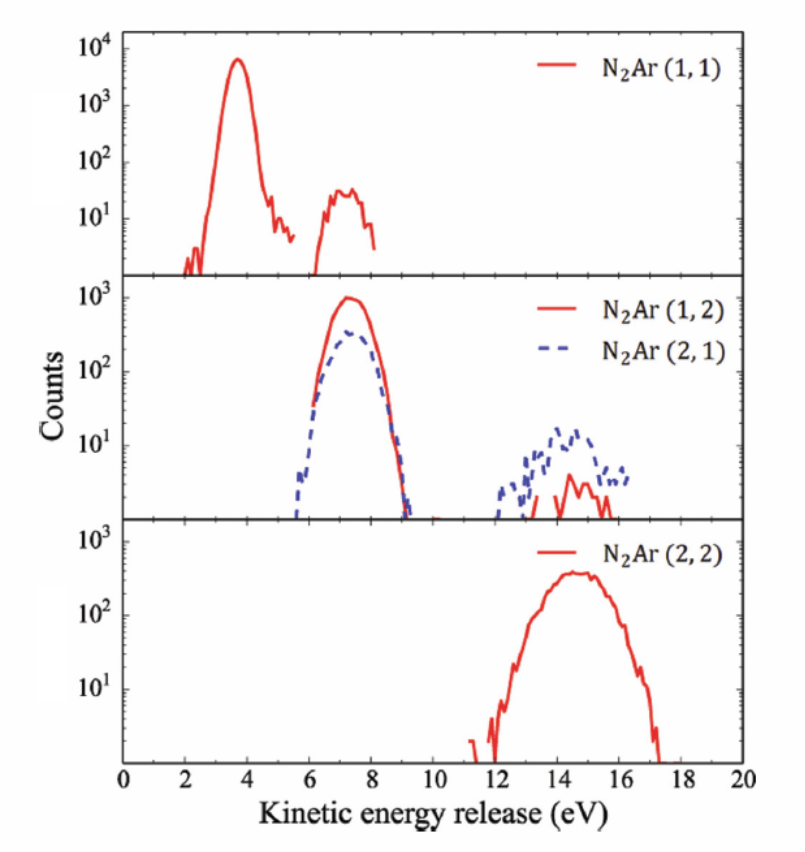

Fig. 3.7. Kinetic energy release spectra of the fragmentation channels of N_2Ar (1,1), N_2Ar (1,2), N_2Ar (2,1), and N_2Ar (2,2) [15].

Fig. 3.7 shows the KER spectra of the different fragmentation channels. For the $N_2Ar(1,1)$ channel, the first peak at 3.7 eV can be assigned to the Coulomb explosion at an internuclear distance between the two constituents of 3.9 Å of N_2Ar^+which is very close to the equilibrium bond length in the N_2Ar molecule of 3.7 Å. Now the reason for the peak locating at 7.2 eV of the fragmentation channel N_2Ar (1,1) will be resolved. Interestingly, as can be seen from Fig. 3.7 that the large peak of N_2Ar (1,2) and N_2Ar (2,1) also lie next to this value, but only slightly higher. This shows a similar behavior as seen in the KER spectra of argon dimer fragmentations in the context of frustrated tunneling ionization. The interesting question here is whether the high peak of $N_2Ar(1,1)$ results from the initial channel N_2Ar (2,1) or N_2Ar (1,2). In the first case the electron would be recaptured by N_2^{2+} and in the second case the electron-recapture would be by the Ar^{2+} ion.

As can be seen in Fig. 3.7, there are two peaks for both fragmentation channels N_2Ar (1,2) and N_2Ar (2,1). These higher peaks are most likely due to the FTI of N_2Ar (2,2) because they show comparable kinetic energy release. Thus it is a proof that both N_2^{2+} and Ar_2+ can recapture the tunneled electron. The former case leads to the high energy peak at N_2Ar (1,2) and the latter one the high energy peak at N_2Ar (2,1). However, the statistics of the high energy peak for the fragmentation channel N_2Ar (2,1) is much higher than the statistics of the high energy peak of N_2Ar (1,2) channel, as can be seen in Table II.

Channels	KER (eV)	Event counts	Recapture probability
N_2Ar (1,1)	3.7	54013	
N_2Ar (1,1)*	7.2	471	3.68%
N_2Ar (2,1)	7.4	4606	
N_2Ar (1,2)	7.4	8186	
N_2Ar (2,1)*	14.4	288	3.49%
N_2Ar (1,2)*	14.4	36	0.43%
N_2Ar (2,2)	14.7	7937	
Ar-Ar (1,1)	3.8	77905	
Ar-Ar (1,1)*	7.3	1841	5.08%
Ar-Ar (1,2)	7.5	36221	
N_2-N_2 (1,1)	3.5	7419	
N_2-N_2 (1,1)*	6.7	13	1.09%
N_2-N_2 (1,2)	6.9	1189	

Table II. The yield ratio and electron trapping probability of fragmentation channels of N_2Ar, Ar-Ar, and N_2-N_2. The electron trapping probability is estimated by normalizing the yield of the electron trapping channel to the total yield of all the channels with the same initial charge state [15].

One can therefore conclude that although the tunneled electron can be trapped by both N_2^{2+} and Ar^{2+}, but the probability of being recaptured by N_2^{2+} is much smaller than that by Ar^{2+}.

3.5 Formation of Zero-Energy States in Laser Fields

In [16], a connection is made between a newly found structure called Zero Energy Structure (ZES) in the photoelectron momentum spectra and the recapture process of frustrated tunneling ionization. Many structures which are observed in the photoelectron momentum spectra measured in experiments cannot be theoretically modeled in the strong field approximation because it neglects the effect of the Coulomb field. The structures termed low-energy structures (LES) and very low-energy structures (VLES) which can be seen in Fig. 10, can be described as Coulomb focusing effects of increasing orders. The zero energy structure however is not a result of the direct effect of the ionization of the electron due to the laser pulse, therefore it does not exist in the simulated picture in Fig. 3.8, because only direct ionizations were modeled in this paper.

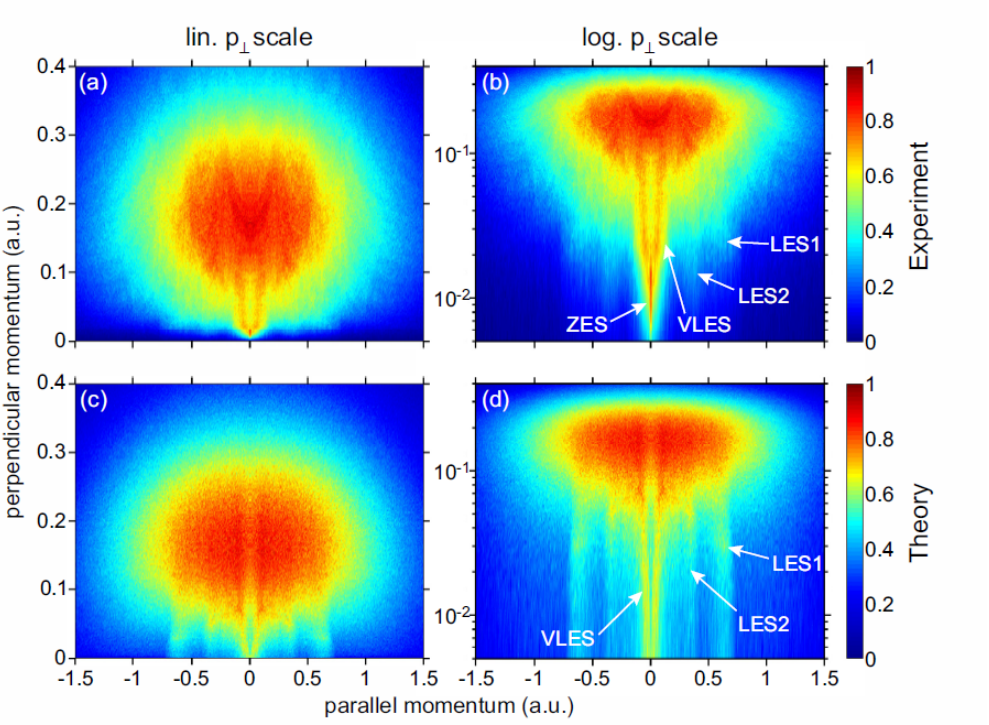

Fig. 3.8. Electron momentum distributions obtained by, measurement (top) and simulations (bottom) for argon after interacting with 68-fs laser pulses with a high peak intensity of $I_0 = 0.9 \times 10^{14}$ W/cm^2 is given with $p\perp$ on linear (left) and logarithmic (right) scales. The first- and second-order LESs (LES1, LES2), the VLES, and the ZES structures are marked [16].

The zero-energy structure (ZES) stems from ionization of electrons which were recaptured into Rydberg states after being initially ionized by the laser pulse, by the weak external DC field in the experimental chamber. The ZES structure is thus a result of the frustrated tunneling ionization mechanism, the recapture of tunneled electrons into bound Rydberg states due the Coulomb field.

4 Experimental Setup

In this section, the experimental setup used to measure the fragmentation dynamics of the argon dimers will be described. The Ti:sa laser system used to produce the femtosecond laser pulses is described in section 4.1. The carrier envelope phase of the pulses is measured with the single shot phasemeter device which will also be briefly introduced in section 4.2. Furthermore a short description of the COLTRIMS technique used in the experiment to measure the the dimensional momentum vectors of all fragmented particles will be given in section 4.3 as well as a method for the preparation of a collimated gas beam with minimal momentum spread which is obligatory for the experiments.

4.1 Laser-System

A 800 nm Ti:sa multipass laser amplifier system which delivers ultashort laser pulses (25 fs, 0.8-1 mJ, 5 kHz) after being recompressed by a double-prism-pair compressor, was used in the experiments [18]. The so called chirped pulse amplification (CPA) technique [6] was used to amplify the laser pulses delivered by an oscillator which is also a Ti:sa laser (7 fs, 3.5 nJ, 80 MHz). CPA is the main technique used to amplify ultrashort pulses. The incident pulse is stretched in time using a positive dispersion medium prior to amplification, thus lowering the intensity to a region where the gain medium is not damaged during the implication process and then recompressed with a negative dispersion compressor back to a short pulse [6]. The main advantage of this technique is the possibility to amplify the pulse to high peak powers without the damaging the crystal and the optics in the system. The amplifier was pumped with another diode-pumped green laser at 532 nm (Nd:YLF). The 25 fs pulses delivered by the amplifier system were further compressed to about 5 fs using the hollow fiber technique [26].

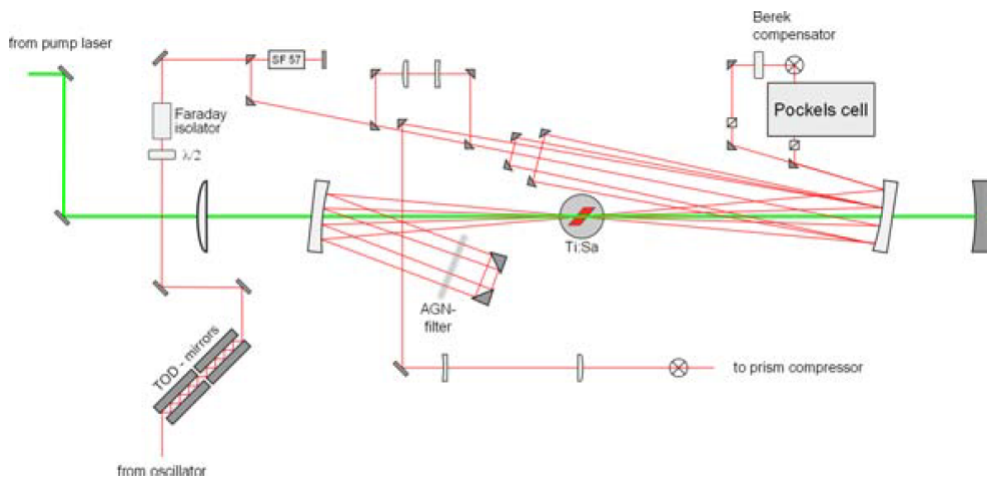

Fig. 4.1. The 10 pass multipass amplifier consists of a 4-pass pre-amplifier and a 6-pass amplifier [18].

Hereby, the laser pulse from the amplifier is sent to a gas filled hollow-fiber where the pulse is spectrally broadened through self phase modulation. Afterwards, chirped mirrors which are specifically designed dielectric mirrors are used to compensate phase distortions arising due to the propagation in the hollow-fiber.

4.2 Phasemeter Device

In this work ionization and fragmentation processes of argon dimers, Ar_2, subject to intense, linearly polarized sub-5 fs laser pulses with a known carrier-envelope offset phase (CEP) are studied. Carrier envelope phase offset results from the relative position difference of the fast oscillating carrier and the slowly varying envelope of the ultrashort pulse due to propagation through media where the group and phase velocity in general can take different values. The electric field $E(t)$ of a few cycle pulse can be described the following way,

$$E(t) = E_0(t)\sin(\omega t + \phi_0) \tag{4.1}$$

where $E_0(t)$ is the envelope of the pulse, ω the carrier frequency and ϕ_0 the carrier

envelope phase. The carrier envelope phase is an important parameter of ultrashort pulses and the one that becomes more important for short pulses as at extremely short durations pulses with different carrier envelope phase (CEP) can have significantly different impact on the target. Therefore the CEP dependence of a specific phenomena can be an interesting topic to explore.

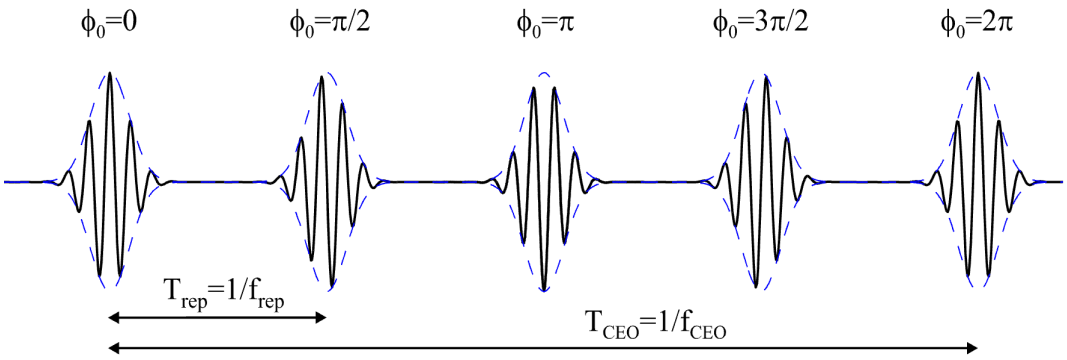

Fig. 4.2. Dependence of the ultrashort laser pulse on its carrier envelope phase offset ϕ_0 where f_{rep} is the repetition rate and f_{ceo} the carrier envelope frequency [24].

A phasemeter device [23] was used to measure the CEP of each and every laser pulse. This device is based on measuring the above threshold ionization (ATI) spectra in two opposite directions. From these spectra the carrier envelope phase of each laser pulse can be calculated and linked to the ion momenta in the off-line data analysis. It was shown in [25] that for short pulses the carrier envelope phase can have a big effect on the ATI spectra of photoelectrons where dependent on the absolute phase more electrons are generated in one or the other direction.

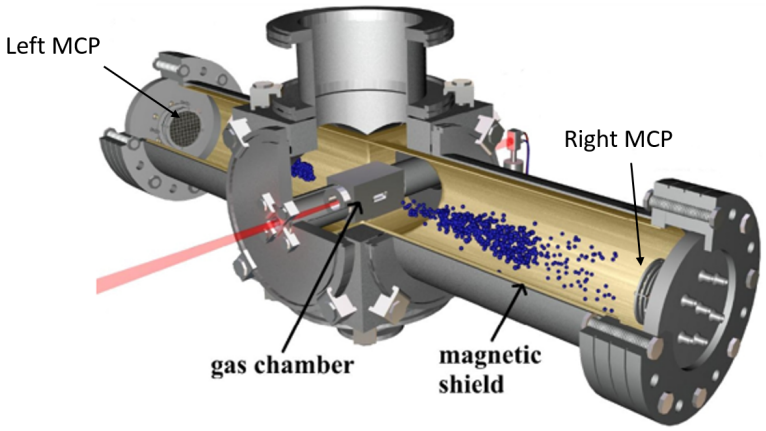

Fig. 4.3. CAD model of a single shot stereo ATI device (phasemeter). Adapted from [19]

With the phasemeter it is possible to measure the CEP of each incoming laser pulse independently. Two detectors denoted as Left (L) and Right (R) are placed on the opposing sides to measure the yield of the photoelectrons impinging on the each detector. By looking at a two particular energy regions denoted as $A_{high} = \frac{L_{high}-R_{high}}{L_{high}+R_{high}}$ showing a sine-like behavior and $A_{low} = \frac{L_{low}-R_{low}}{L_{low}+R_{low}}$ showing a cosine-like behavior, a parametric plot ("phase potato") can be obtained by plotting A_{high} versus A_{low}. An example of the "phase potato" plot gained is shown in Fig. 4.4.

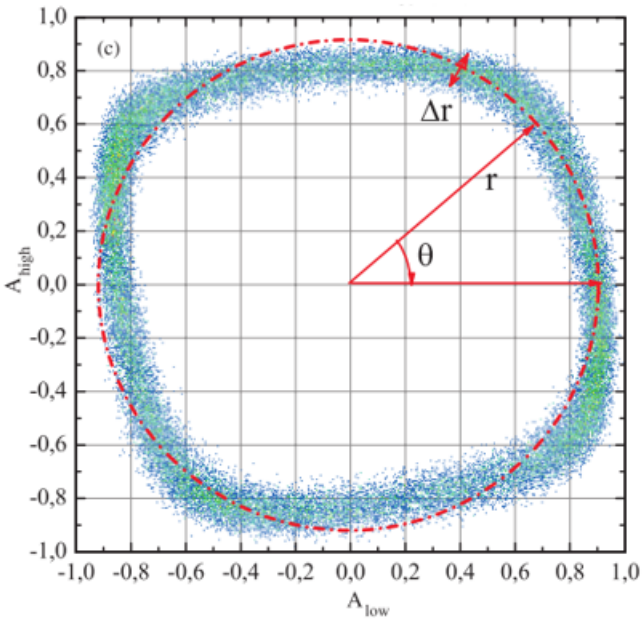

Fig. 4.4. Parametric asymmetry plot where A_{high} is plotted versus A_{low}. Adapted from [19]

In general the measurable quantity (polar angle in the parametric asymmetry plot) θ and the CEP ϕ have a roughly linear relationship but in many cases the phase potato will not have a constant radius r and would not be uniformly distributed in θ. However, one can show that [23],

$$d\phi = \frac{\rho(\phi)}{\langle\rho\rangle} d\phi = \lambda(\theta) d\theta \rightarrow \phi(\theta) = \phi_0 + \int_0^\theta \lambda(\theta') d\theta' \tag{4.2}$$

where $\rho(\theta)$ is the density and $\langle\rho\rangle$ the average density of the laser shots, respectively as a function of θ. In these cases the CEP $\phi(\theta, r)$ which depends on θ and r must be retrieved from the measured results. Fig. 4.5 shows a parametric asymmetry plot measured in the experiments on FTI in Ar_2 (section 5.3). A CEP retrieval algorithm based on Eq. 4.2 was used to retrieve the carrier envelope phase from the measured data.

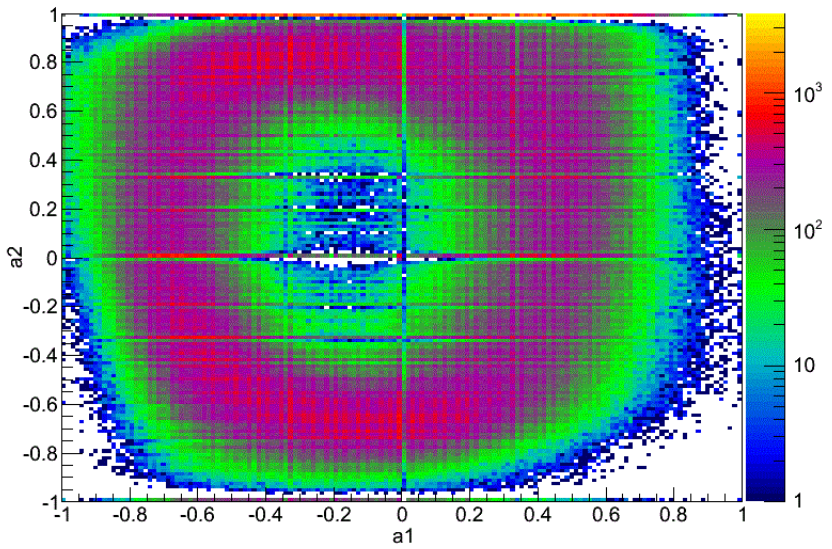

Fig. 4.5. Phase potato of the fragmentation channel Ar^+-Ar^+. The axis labels a1 and a2 stand for A_{high} and A_{low}.

Fig. 4.6 - 4.8 show the phase potatoes with different kinetic energy release peak selections for the fragmentation channel Ar^+-Ar^+. The plots show that the CEP

retrieval was successful as the dependence between the angles θ and ϕ is linear.

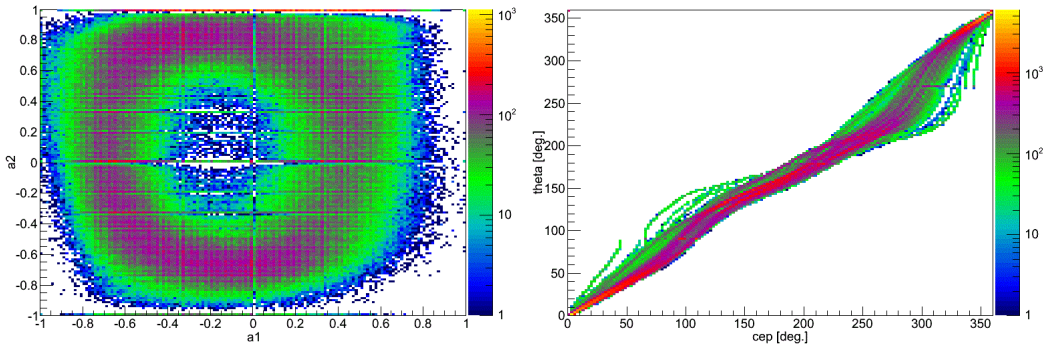

Fig. 4.6. Phase potato of the fragmentation channel Ar^+-Ar^+ with the KER selection of the coulomb explosion peak. The axis labels a1 and a2 stand for A_{high} and A_{low}.

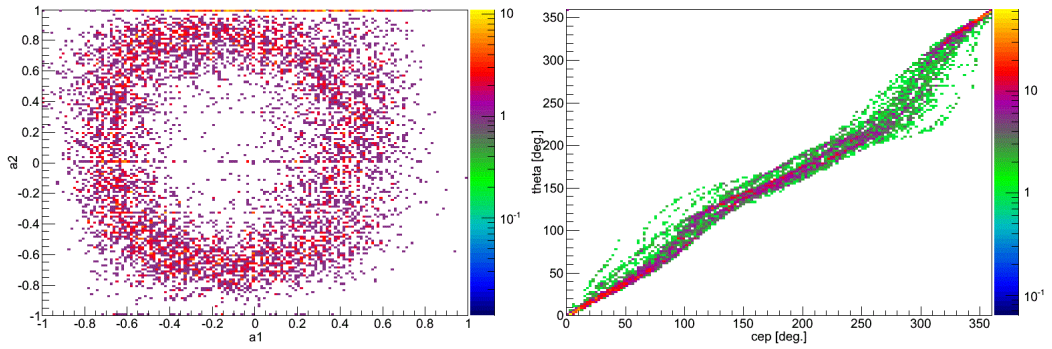

Fig. 4.7. Phase potato of the fragmentation channel Ar^+-Ar^+ with the KER selection of the second KER peak at 5.3 eV. The axis labels a1 and a2 stand for A_{high} and A_{low}.

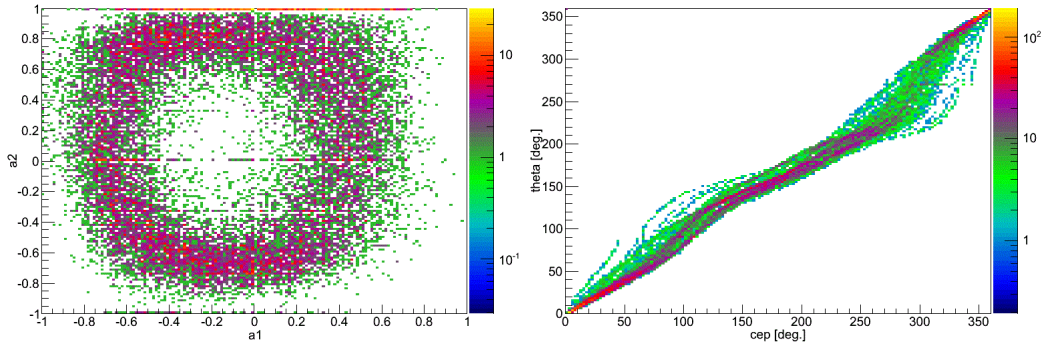

Fig. 4.8. Phase potato of the fragmentation channel Ar^+-Ar^+ with the KER selection of the frustrated tunneling ionization peak 7.2 eV. The axis labels a1 and a2 stand for A_{high} and A_{low}.

4.3 COLTRIMS

Cold Target Recoil Ion Momentum Spectroscopy (COLTRIMS) is an imaging technique pioneered at the University of Frankfurt [29] and Kansas State University which nowadays is deployed in various groups around the world to measure the electron and nuclear dynamics of atoms and molecules. It allows one to measure the three dimensional momentum vectors of the fragmented particles from collision experiments. Among other uses, one can explore with this technique the induced Coulomb explosion processes after laser matter interaction [17-19,22,29].

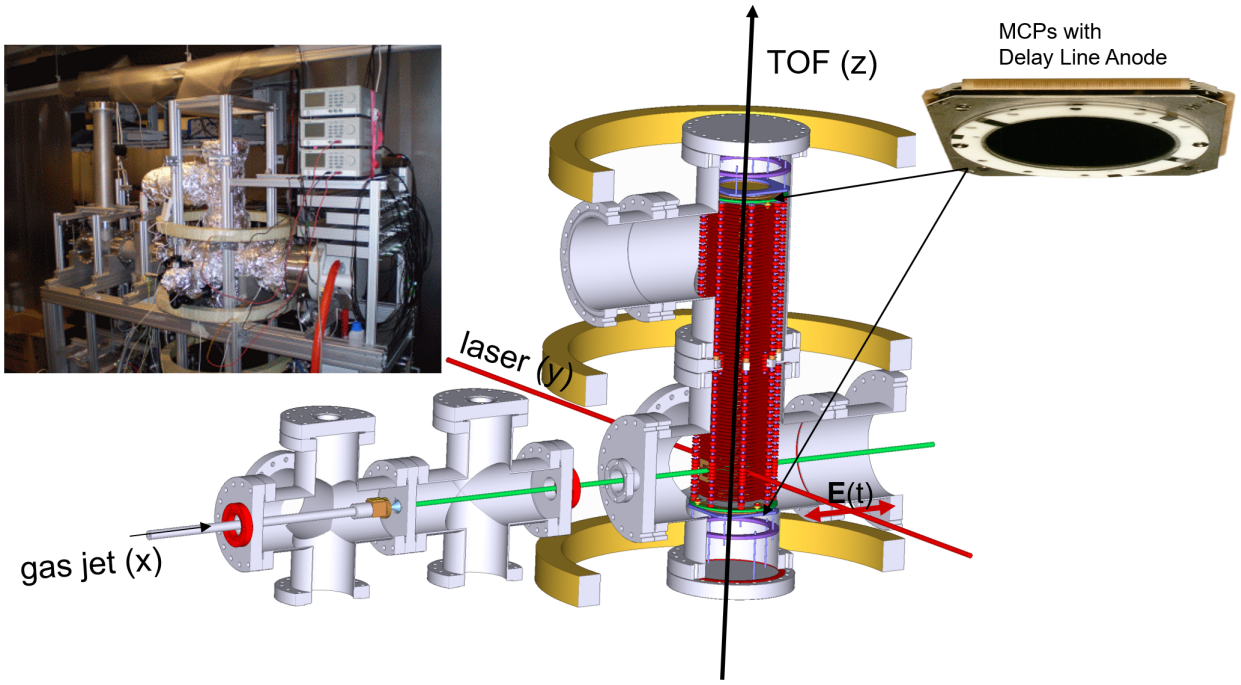

Fig. 4.9. Schematic of the COLTRIMS setup modeled with CAD. The inlet shows the working setup. Adapted from [19]

In the COLTRIMS chamber the projectile beam, which can consist of charged particles, photons or electrons, interacts with the beam of atoms or molecules. Depending on the experiment, the projectile beam and the molecular beam are varied. In our experiments we use ultrashort laser pulses with a 5-fs (FWHM) temporal duration as the projectile beam, and a cold gas jet with argon atoms, dimers, trimers as the molec-

ular beam. The two beams intersect at 90°. The overlapping volume of the two beams is called the reaction zone. Electrons and charged particles which are formed due to the interaction are driven to the micro-channel plates (MCP) detectors with high spatial and temporal resolution, using electric and magnetic fields. The two detectors in the COLTRIMS chamber are placed opposite to each other. Therefore, the negatively charged electrons and the positively charged ions impinge on the opposing detectors respectively, given the same electrostatic field.

The experimental chamber is kept under high vacuum (10^{-10} mbar). This is important for the following reasons: the MCPs need good vacuum to work properly, the supersonic gas expansion would not be possible otherwise and most importantly, collisions with other gas particles must be avoided. For each impinging particle on the detector, the impact spot (x, y) is measured. Additionally, the time-of-flight (tof) of the fragmented particles which is the time between the laser-matter interaction and the arrival of the particles on the detector, is measured. With these three coordinates (x and y from the impact spot on the detector; z from tof) it is possible to reconstruct the momentum vector $\mathbf{p} = (p_x, p_y, p_z)$ of each fragmented particle by defining: $p_x \equiv x$, $p_y \equiv y$, $p_z \equiv tof$. Furthermore, it is an easy step to calculate the KER once the momenta are known. One can estimate the total energy release after a two body fragmentation with the momenta $\mathbf{p_1} = (p_{1x}, p_{1y}, p_{1z})$ and $\mathbf{p_2} = (p_{2x}, p_{2y}, p_{2z})$ of each particle respectively, as follows:

$$KER = \frac{\mathbf{p_1}^2}{2m} + \frac{\mathbf{p_2}^2}{2m}. \tag{4.3}$$

The measurement of tof further allows us to make a clear distinction in terms of particles with different mass and charge in the off-line analysis. With the measurement of the momentum vectors of (almost) all fragmented particles, it is possible to "replay" the dissociation processes in an off-line analysis on the computer which is one of the main strengths of COLTRIMS.

The acquired signals are saved in the so called LMF (list-mode) files. The measured

coordinate triplets of the particles are saved as one event into the listmode file. All coordinate triplets measured from both the electron and ion detector at the same time, which is limited by the temporal resolution of the detector, are listed under one event. The listmode file consists therefore of a stack of all the measured events. In the off-line analysis on the computer one can access all the measured events and are therefore capable to filter relevant incidences from the rest [18].

4.3.1 Argon Dimer Gas Jet

To resolve small momentum variations due to the fragmentation processes, a well defined initial momentum of the target gas particles is needed. In our experiments a argon gas jet which consisted mainly of argon atoms but also a small percentage (2-3%) of argon dimers and a very small percentage of argon trimers was used. The jet was then sent through a thin nozzle after which a supersonic gas expansion took place. During the supersonic expansion, the internal thermal energy of the gas particles is transformed into directional translational energy. This leads to an effective cooling of the gas particles. The pressure in the expansion chamber must be much smaller than the initial pressure for the supersonic expansion to take place. Due to the interaction of the expanding gas particles with the residual gas particles inside the chamber various zones are formed especially a so called "zone of silence" which corresponds to the mean free path of the particles in the chamber.

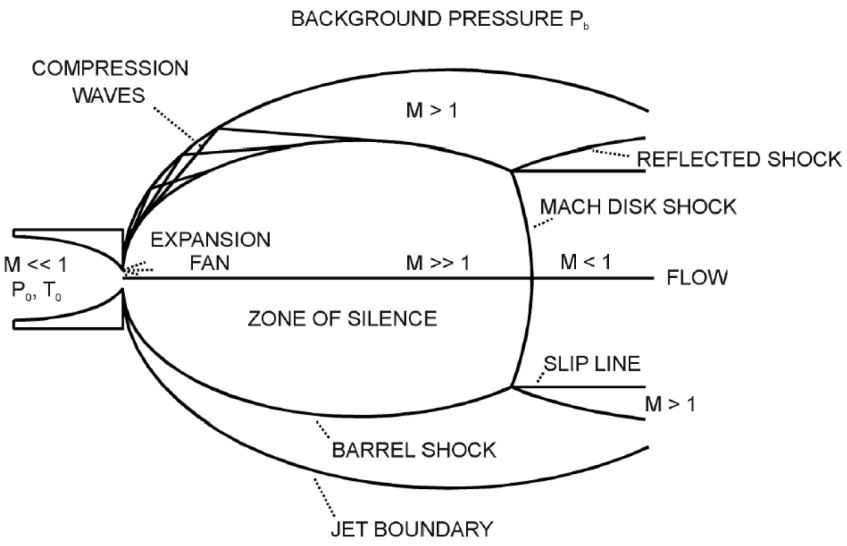

Fig. 4.10. Schematic of the supersonic gas expansion [30]

Inside the zone of silence the particles can propagate without colliding with other particles. Into this zone of silence a so called skimmer is placed which enables to cut out a well localized beam with minimal momentum spreading. To reach smaller temperatures, it is possible to "pre-cool" the gas particles prior to the supersonic gas expansion.

4.3.2 Spectrometer

A well adjusted time of flight (ToF) spectrometer is important for the COLTRIMS setup. It is highly important to have homogeneous fields in the reaction chamber since the trajectory of the particles depend on them. Even small distortions to the fields during the experiment can lead to imprecise results. Depending on the voltage applied to the spectrometer and therefore the generated electric field in the chamber, the ions and electrons are driven to different detectors on each side of the spectrometer. The static electric field is set along the z-axis, therefore the x and y components of the particle momenta are not altered due to the field but they are accelerated along their z-axis due to the force $ma_z = qE$ acting on them because of the field, where m and q are the mass and the charge of the particles, respectively. E is the electric field

and a_z the z-component of the acceleration $\mathbf{a}$. Therefore, one can see that tof of the particles depend on their mass and charge leading to a mass-resolved spectrum also in case of particles with the same charge. It can be shown that the time of flight (tof) is proportional to the square root of the mass of the particle, $tof \propto \sqrt{m}$. Therefore, heavier atoms take longer to reach the detector. The square root of electric field E and the square root of the charge state q of the atoms are on the other side inversely proportional to time of flight, $tof \propto \sqrt{\frac{1}{qE}}$. This can be used to find the exact electric field in the chamber. By checking the ToF spectrum of a noble gas, for example argon which consists of several peaks depending on the laser intensity one can attribute these peaks to different charge states. By plotting tof versus $\sqrt{m/q}$ one can find the exact electric field inside the chamber [17].

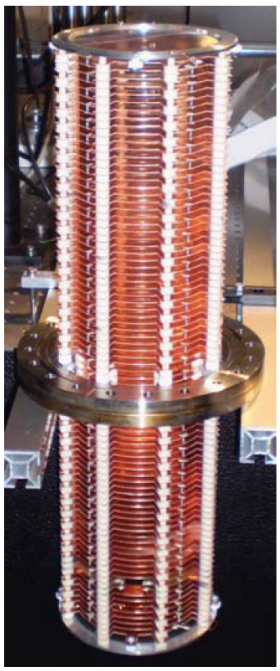

Fig. 4.11. Photo of the COLTRIMS spectrometer. Using stainless steel meshes the spectrometer is closed on both ends. Eight ceramic rods are used to stabilize and support the construction [18].

The spectrometer contains 86 copper plates that are equidistantly spaced. The inlets of target and laser beam into the reaction chamber divide the spectrometer into a long upper part and a short lower part. The advantage of this choice is that it allows one to study molecular fragmentation and atomic ionization processes in the

same spectrometer. A higher resolution can be achieved with long spectrometers in case of atomic ionization processes. For molecular fragmentation processes a short spectrometer is better suitable as it reduces the smearing. This can be achieved by simply changing the sign of the applied voltage depending on the experiment.

4.3.3 Detector

Detectors with high spatial and time resolution are needed to measure with the precision required for our use in coincidence spectroscopy. The main components of the detectors are micro-channel plates (MCPs) and a delay line anode. The micro-channel plates are electron multipliers which make a measurable signal out of initially single impinging particles. It intensifies the initial signal by multiplication of electrons via secondary emission.

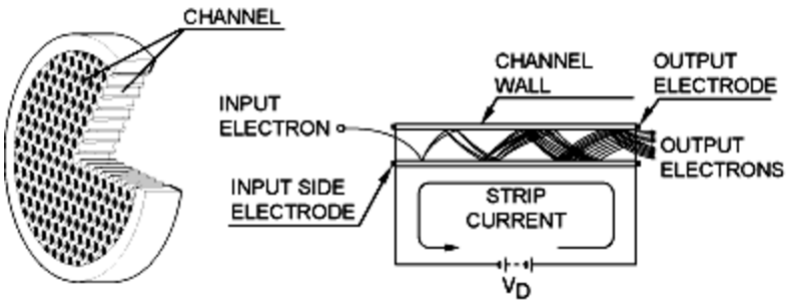

Fig. 4.12. Schematic of a micro-channel plate (MCP) [20].

A micro-channel plate is a slab which consists of a parallel array of glass tubes which are densely distributed over the whole surface. As the electrons on the surface have a small work function, even particles with low energies can induce ionization. These electrons are accelerated using high voltage inside the MCP and they induce further secondary electrons leading to an electron avalanche signal.

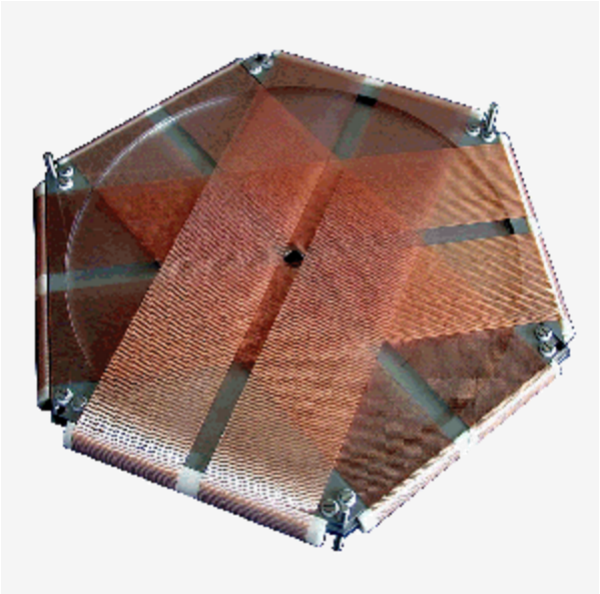

Fig. 4.13. Photo of a delay line anode. Three layers of copper wires are wound up to increase the detecting efficiency [28].

This electron cloud is then accelerated with an applied field on to the delay line anode made out of a wound up copper wire. The delay line anode is used to gain the spatial information of the impact. Three layers (u,v,w) of copper wires rotated 60° to each other are used to increase the detecting efficiency. The third layer is not necessary as it delivers redundant information, but is useful to reconstruct the events in case signals from the other layers are lost. The electron avalanche reaches the copper wire of the delay line anode and induces an electric signal, which travels to both ends of the wire. As the wire length is a known quantity, we can reconstruct from the arrival times of the two signals the impact position on the delay line anode. Due to smearing the electron cloud usually induces the signal on more than one wire. In total, seven detector signals are recorded per event: six signals from the ends of the anode (each layer delivering two signals) and one from the MCP impinging spot.

5 Data Analysis and Results

One of the key objective of this work is to observe the carrier envelope phase dependence of the frustrated tunneling ionization process. Experiments were conducted using three different laser intensities, which will be in the following denoted as high, intermediate and low intensity. All three intensities were in the tunneling regime of the strong-field laser ionization. The estimated peak intensity was $I_{intermediate} \approx 10^{15}$ W/cm^2 for the intermediate intensity. The results obtained with the intermediate intensity were the most informative as we received the highest statistics for the frustrated tunneling ionization process with this intensity. Therefore analysis was mostly concentrated on the data gained from measurements with the intermediate intensity. In the experiments, more than 1.7 billion fragments were detected, from which only a couple of thousands were involved in this electron recapture processes.

The raw data in the LMF files were converted into ROOT files for further analysis. ROOT is an open source software package developed at CERN to analyze large data sets to obtain and filter relevant information from the raw data and for further visualization tasks.

5.1 Detector and Electric Field Calibration

As already discussed, it is possible to use the raw data to calibrate the detector and the electric field in an off-line analysis. The software package LMF2ROOT written in C++ is used to convert the information from the measured signals into meaningful physical quantities. However, before it is possible to calculate the physical quantities it is important to pre-assort the relevant measured values by removing redundancies and errors. Possible measurement errors could be caused by irrelevant electronic signals which would be registered as an ionization event. This sort of error can be removed if the time moment of detection exceeds the maximum time for an electronic signal to reach the anode. The cut-off time is a constant that can be precisely estimated because the length of the anode is known. Signals which have a shorter duration are the only

relevant ones. Another possible error could occur when many particles trigger anode signals close to each other so that it is not feasible to establish a two particle correlation. This problem can be circumvented by looking at the sum of the time durations at the anode ends of both pulses which is independent from the impact spot on the anode. Fig. 5.1 and Fig. 5.2 show histograms where the time sum of the of the u-layer of the delay line anode is plotted with raw data and the calibrated data.

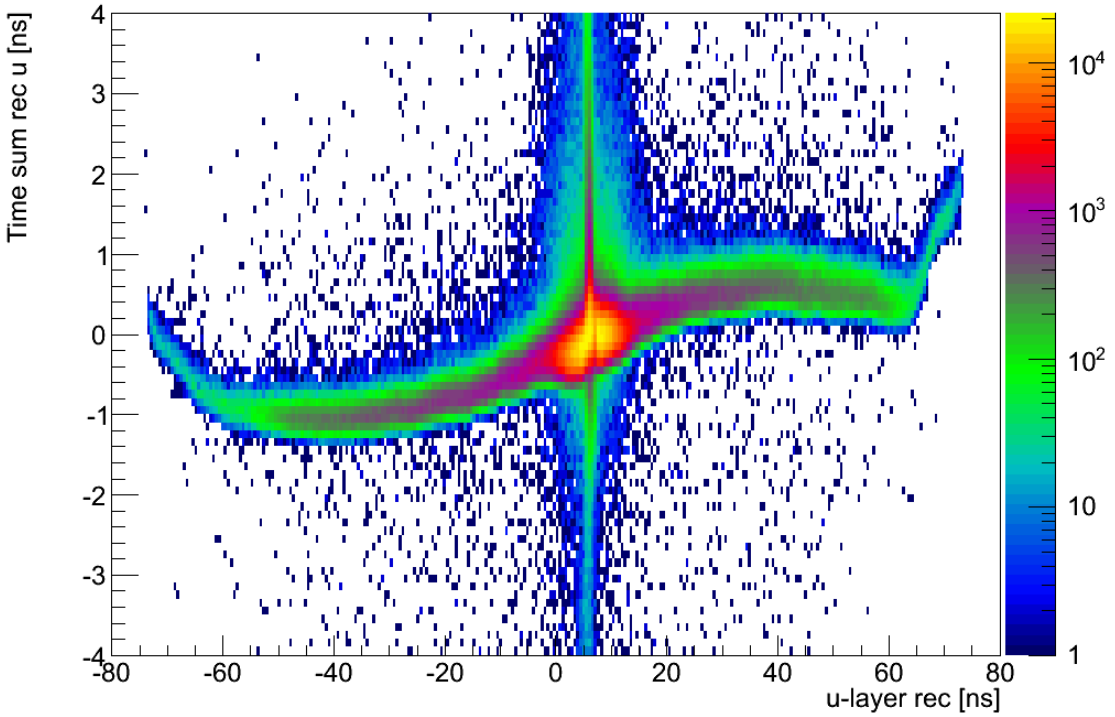

Fig. 5.1. Time sum of the u-layer of the delay line anode with raw data. The plot shows that the time sum is not calibrated and takes nonzero values.

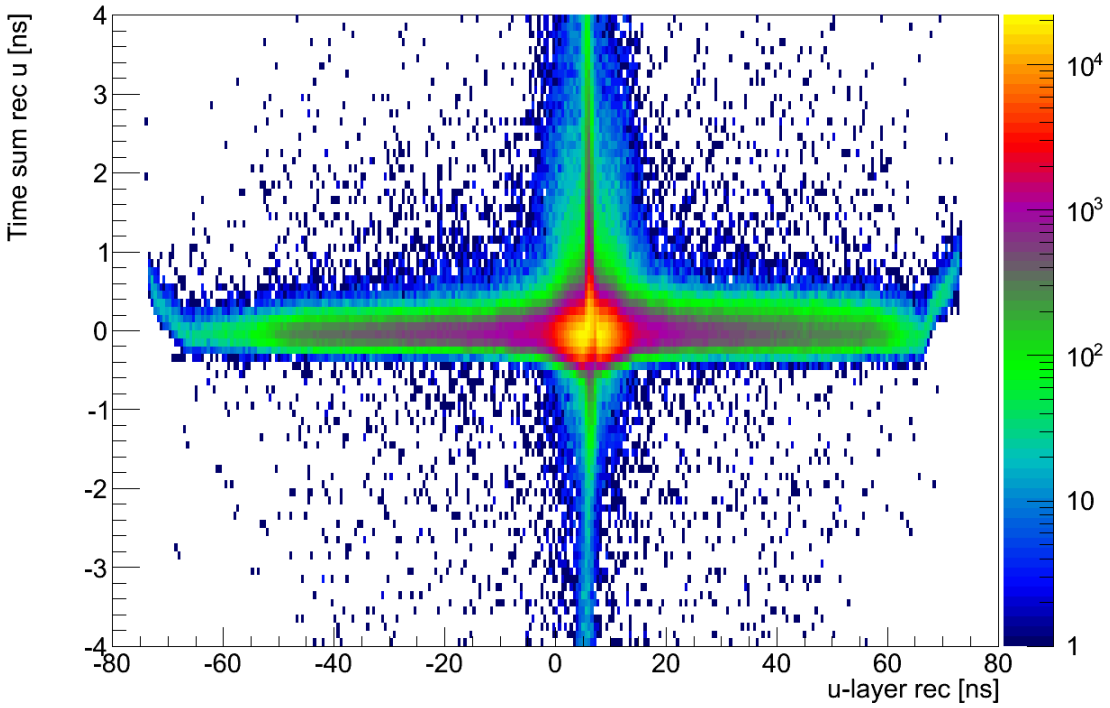

Fig. 5.2. Time sum of the u-layer of the delay line anode with calibrated data. The plot shows that the time sum is calibrated as the time sum takes values close to zero.

Due to measurement inaccuracies in the length of the spectrometer which is needed to calculate the electric field and the fact that it is not possible to estimate the correct reaction spot which varies in each experiment, it is important to calibrate the electric field in the spectrometer before further analysis can be conducted. To calculate the electric-field the time-of-flight of two different known particles is examined and compared with the theoretical values for the electric field which would correspond to this specific tof. Using the time of flight spectrum shown in Fig. 5.3 it is possible to identify the time of flight of the different particles as they appear as sharp peaks in the spectrum. In the data analysis, the peak resulting from the Ar^{+} and Ar^{2+} ions were used to calibrate the electric field in the spectrometer.

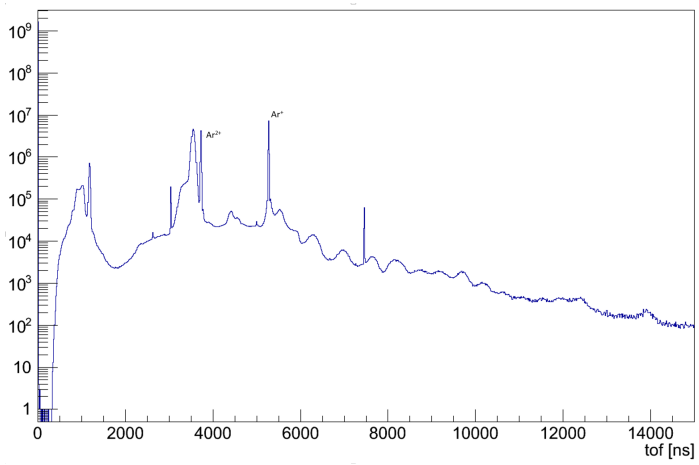

Fig. 5.3. Time of flight (ToF) spectrum. The sharp peaks can be unambiguously assigned to different fragments.

After ensuring that all errors are removed, the momentum distribution was centered with respect to the coordinate system in a last step. Correlated processes can be visualized using the so called Photo-Ion Photo-Ion Coincidence (PIPICO) spectrum. In this plot, the time of flight of two measured particles is plotted: the time of flight of one particle versus the time of flight of the second particle. The resulting plot nicely visualizes all ionization processes. Moreover, one can clearly identify the correlated processes where the two particles originate from a fragmentation process and therefore formed at the same time. The corresponding events must be selected by filtering out the data which do not correspond to a correct type of correlation. In the PIPICO plot these correlated events are shown as the curves. Fig. 5.4 shows the PIPICO spectrum measured in the experiments.

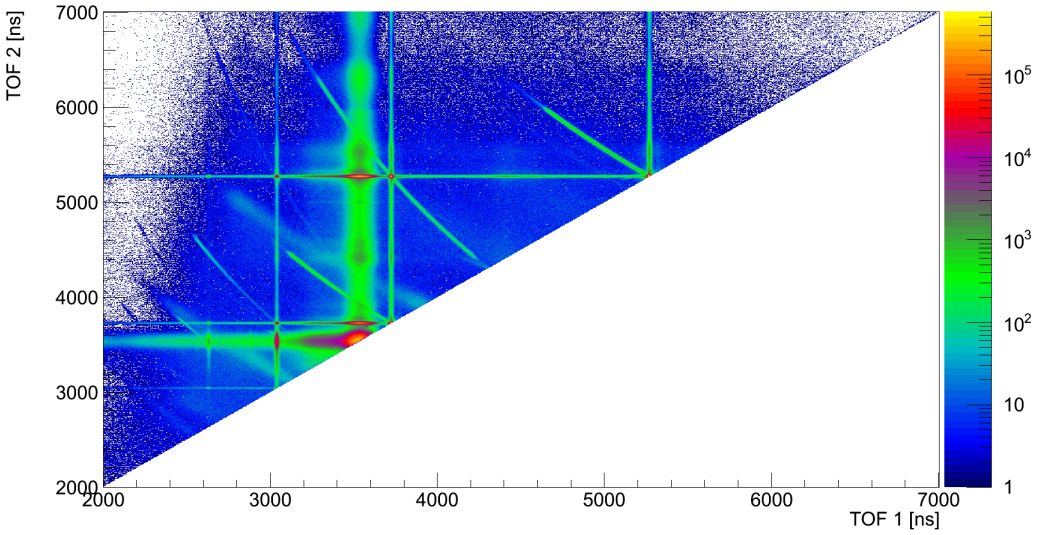

Fig. 5.4. Photoion-Photoion coincidence (PIPICO) Plot. Time of flight on one fragment is plotted against the time of flight of the second fragment. The curved lines correspond to correlated two body events and the straight lines to atomic ionization processes.

5.2 Kinetic Energy Release (KER) Spectra

In this section the results gained from the experiments with intermediate intensity will be presented. Following fragmentation channels were considered in the analysis with two symmetric ones and two asymmetric breakup channels. The laser pulse ionizes an argon dimer leading to its subsequent fragmentation due to Coulomb repulsion between the ions. The equations below describe the explosion of the ionized argon dimer leading to different fragmentation channels depending on the initial state.

$$Ar_2^{2+} \rightarrow Ar^+ + Ar^+ \Longrightarrow Ar(1,1) \tag{5.1}$$

$$Ar_2^{3+} \rightarrow Ar^{2+} + Ar^+ \Longrightarrow Ar(2,1) \tag{5.2}$$

$$Ar_2^{3+} \rightarrow Ar^+ + Ar^{2+} \Longrightarrow Ar(1,2) \tag{5.3}$$

$$Ar_2^{4+} \rightarrow Ar^{2+} + Ar^{2+} \Longrightarrow Ar(2,2) \tag{5.4}$$

The difference between the fragmentation channels given in Eq. 5.2 and Eq. 5.3 is that in the first case the Ar^{2+} ion is detected first, whereas in the other case Eq. 5.3, the Ar^+ ion is detected first. In the following, density plots of the magnitude of the

vector momentum sum corresponding to the fragmentation channels versus their KER are shown. This allows us to distinguish between real and random coincidences. If two ions originate from the same argon dimer, their sum momentum will be close to zero and therefore lie in a stripe near zero sum momentum.

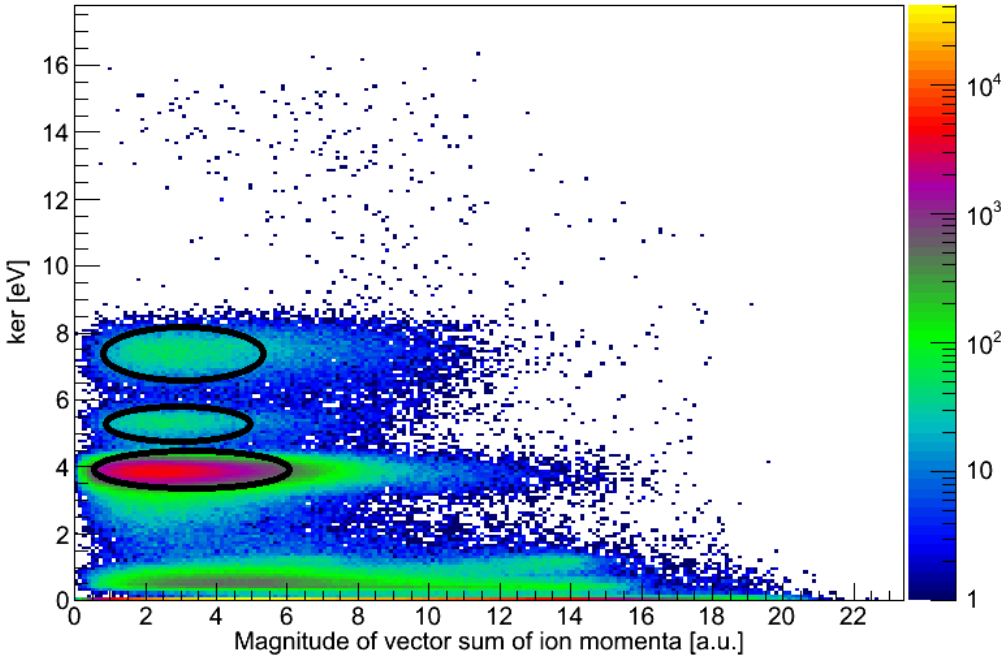

Fig. 5.5. Density plot of the magnitude of the vector momentum sum of the argon ions versus their KER for the Ar^+-Ar^+ dissociation channel Ar(1,1).

In Fig. 5.5, there are three distinct structures (emphasized with the black circles) in the density plot, which correspond to the three peaks in the KER spectrum (Fig. 5.8). The features below 2 eV stem from argon atom ionization processes and are not relevant to dimer fragmentation processes. The long "tail" at ~ 4 eV could be a result of argon trimer dissociating into two singly charged a neutral charged argon atom with very small momentum.

In Fig. 5.6, we see two distinct structures at ~ 7.4 eV and 14.2 eV, corresponding to the Coulomb explosion peak and the electron recapture FTI peak, respectively. We can also see in Fig. 5.6, that the two electron recapture signal (around 21.1 eV) is very weak. Structures which can be seen below 3 eV and above $\sim$10 a.u. of $|\overrightarrow{p}|$ are artifacts and relate to processes not corresponding to two body fragmentations. Furthermore

the strong peak at 10.1 eV is an artifact.

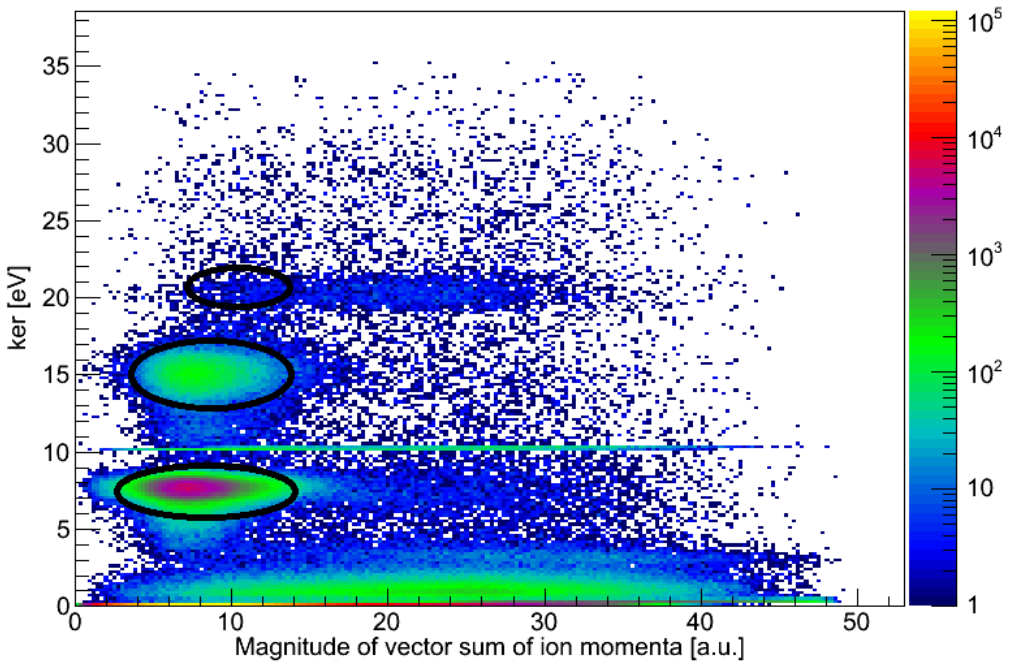

Fig. 5.6. Density plot of the magnitude of the vector momentum sum of the argon ions versus their KER for the combined Ar^{2+}-Ar^{+} and Ar^{+}-Ar^{2+} dissociation channels Ar(2,1) and Ar(1,2).

In Fig. 5.7, we see again two distinct structures at around 14.4 eV and 21.8 eV which correspond to the two KER peaks (Fig. 5.8). The structure at 20 eV is an artifact which does not correspond to any real physical quantity.

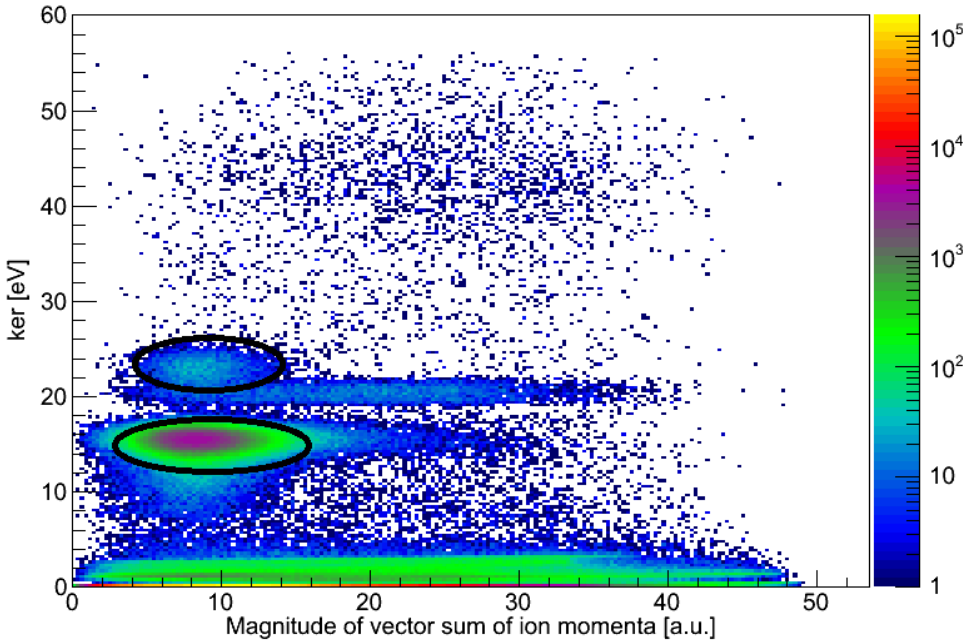

Fig. 5.7. Density plot of the magnitude of the vector momentum sum of the argon ions versus their KER for the Ar^+-Ar^+ dissociation channel Ar(2,2).

The frustrated tunneling ionization process is denoted by *. A double-recapture, i.e. the recapture of two electrons is denoted by 2*. Due to the nature of the FTI mechanism, the fragmentation processes denoted by $Ar^*(n,m)$ and $Ar^{2*}(n,m)$ appear as peaks in the KER spectrum of the $Ar(n,m)$ fragmentation channel. This is because the recaptured electron is in a high lying Rydberg state with a large spatial extension [12-14]. Therefore, this electron only weakly shields the ionic charge. As a result, the unexcited argon ion senses an opposing charge that is effectively higher by one (two) for a single (double) recapture process. Consequently, the energy released during the Coulomb explosion process is that of an argon dimer in an ionic state higher by one (two). On the detector, however, the excited argon ion is measured with its nominal charge. Therefore, a recapture process is unambiguously identified by higher energy peaks in the KER distribution.

In Fig. 5.8, the KER spectra of the different channels are shown. Similar results were reported in [12-14] as summarized in section 3.3, although the spectra measured with few-cycle pulses show subtle differences to those reported with long pulses. In-

terestingly, we measure a higher yield for the trapped Rydberg electrons. Another interesting aspect is the emergence of the KER peak at 5.3 eV in the fragmentation channel Ar(1,1) also after interaction with few-cycle pulses. Electron recapture is not the reason for this peak but several other mechanisms were proposed. We also measure a KER peak corresponding to a double electron recapture process in the Ar(2,1) fragmentation channel, as was observed in [14].

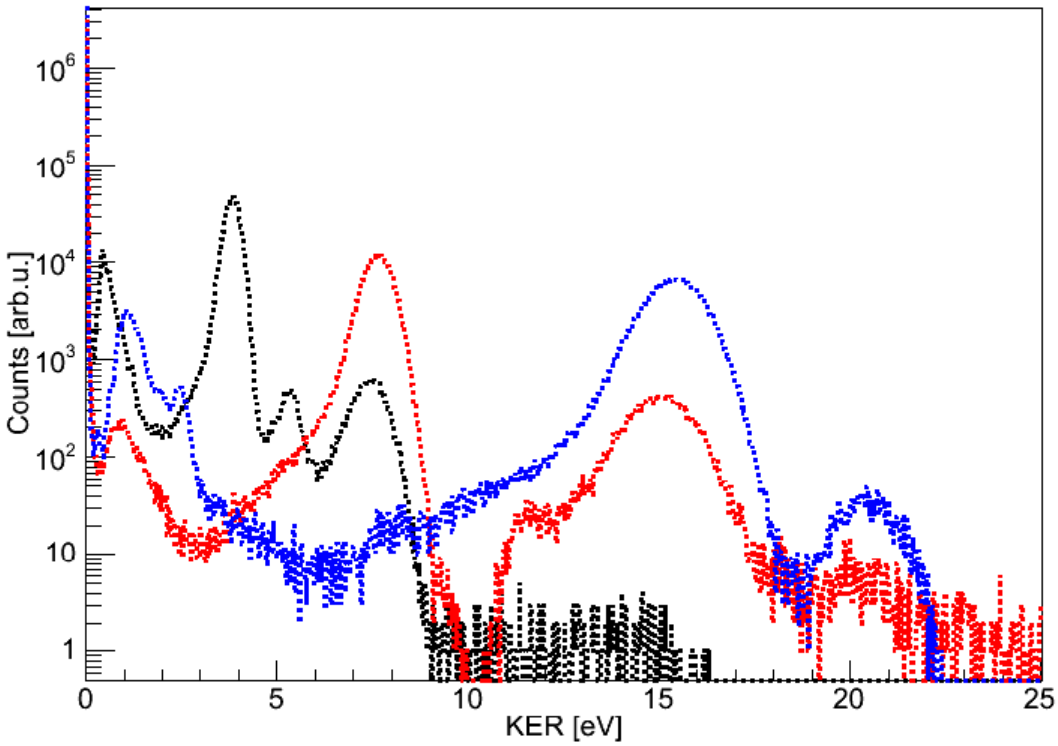

Fig. 5.8. Kinetic energy release (KER) spectra of the fragmentation channels (Eq. 4.1 to 4.4) with intermediate intensity with logarithmic scale. The black line shows the KER of channel Ar(1,1), the red line Ar(2,1) and the blue line Ar(2,2).

For the channel Ar(1,1), KER peaks at 3.7 eV, 5.2 eV and 7.2 eV are measured, as can be seen in Fig. 5.8 (black line). The highest peak at 3.7 eV corresponds to the Coulomb explosion of the argon dimer. The main difference in the parameters of our experiments and the published data is the laser pulse duration. The interaction with a 5-fs laser pulse proceeds quite differently than in the case of a longer laser pulse. The third peak at 7.2 eV is attributed to frustrated tunneling ionization where the electron

recapture process leads to neutral fragments at high Rydberg states. From an initial configuration Ar^{2+}-Ar^{+}, the Ar^{2+} ion recaptures a tunneled electron, resulting in a coincidence breakup.

For the channels Ar(2,1) (Fig. 5.8. red line), peaks centered at 7.4 eV, 14.2 eV and 21.1 eV were measured. Remarkably, the Coulomb explosion peak at 7.4 eV of the Ar(2,1) and Ar(1,2) channels correspond well to the FTI peak of Ar(1,1). This can be expected as both peaks are the result of the fragmentation of an argon dimer with the same initial charge but in the case of FTI one electron is recaptured leading to a slightly smaller KER. Further peaks are found at 14.2 eV and 21.1 eV. The peak at 14.2 eV could be a result of the FTI mechanism, where after an initial configuration Ar^{2+}-Ar^{2+}, one of the two argon ions recapture a third tunneling electron, leading to this peak in the KER spectrum. The most interesting peak is located at 21.1 eV. As discussed in section 3.3, it was proposed [14] that also more than one electron can be recaptured in the context of frustrated tunneling ionization. It is possible that the peak in our data at 21.1 eV could be a result of such two electron recapture. In this case from an initial configuration Ar^{3+}-Ar^{2+}, two more electrons are tunnel ionized but both of them will be recaptured by the argon ions leading to this peak in the KER spectra of the Ar(2,1) fragmentation channel.

For the channel Ar(2,2) (Fig. 5.8. blue line), peaks at 14.4 eV and 21,8 eV were measured. The peak at 14.4 eV results from a Coulomb explosion. The existence of the Coulomb explosion peak at 14.4 eV corroborates the assumption that the peak at 14.2 eV in the Ar(2,1) channel stems from the FTI mechanism. The small energy shift of 0.2 eV can be explained as the result of the charge screening of the ion by the recaptured Rydberg electron. Therefore the Coulomb repulsion between the two ions decreases after the localization of the electron on one of the two ions leading to a slightly smaller KER. The peak at 21.8 eV results from an electron recapture process, where from a initial configuration Ar^{3+}-Ar^{2+}, the argon ion with the higher charge Ar^{3+} recaptures the tunneled electron.

5.2.1 Angular Dependence of the KER peaks

In this section, we examine whether the direction of the argon dimer with respect to the laser polarization direction has an effect on the KER peaks of the fragmentation channel Ar^+-Ar^+. The angle θ is defined as the angle between the laser polarization direction and the axis of the argon dimer at the instant of fragmentation. A value close to one for $\cos(\theta) \sim 1$ indicates that the argon dimer was oriented parallel to the laser polarization direction and therefore $\cos(\theta) \sim 0$ means that the argon dimer was oriented perpendicular to the laser polarization direction.

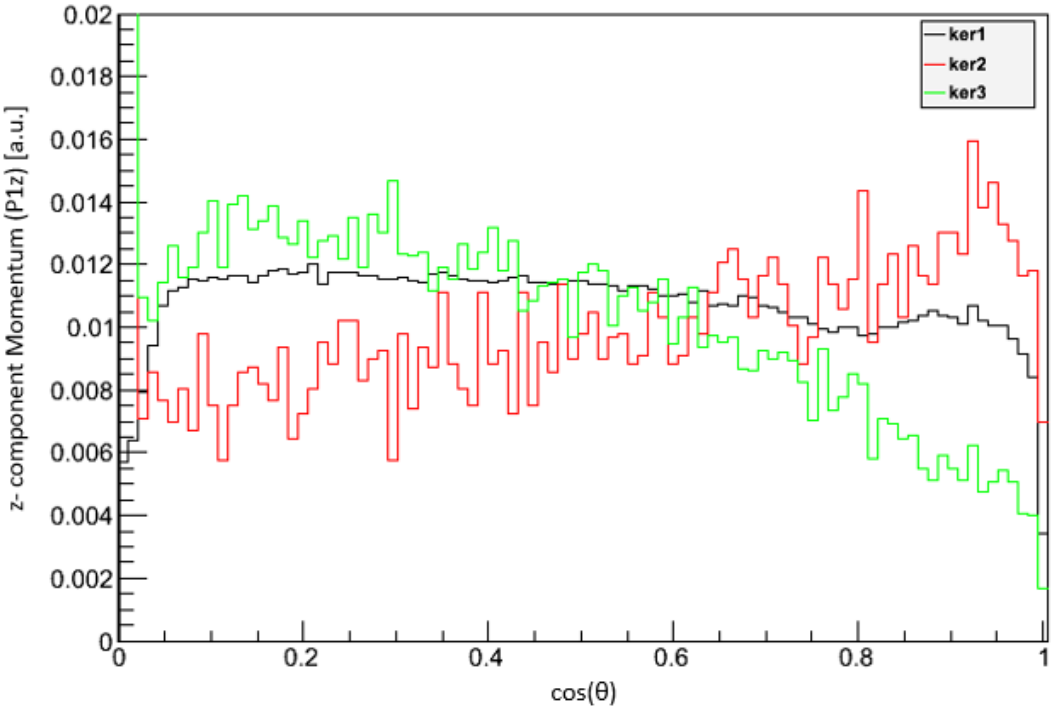

Fig. 5.9. Yield of the particles with different KER selections depending on the orientation of the laser polarization direction. The laser polarization direction is parallel to the dimer orientation for $\cos(\theta) = 1$

Fig. 5.9 shows that the three KER peaks, where ker1 corresponds to the coulomb explosion peak at 3.6 eV, ker2 corresponds to the KER peak at 5.2 eV and ker3 corresponds to the highest frustrated tunneling ionization peak at 7.2 eV, show a pronounced difference in their dependence on the direction of the argon dimer. Most interestingly, the

frustrated tunneling ionization peak (green line in Fig. 4.9) is more likely to originate from argon dimer fragmentation processes where the dimer is oriented perpendicular to the laser polarization direction. This is consistent with the proposed FTI theory [10-14] which predicts that probability for electrons to be tunnel ionized on the maximum of the laser field is higher for argon dimers which are oriented perpendicular to the laser polarization direction. Furthermore the electrons that tunnel close to the maximum of the electric field do not gain enough energy from the laser field and are more likely to be recaptured by the parent ion.

5.2.2 Yield Ratio and Electron Recapture Probability

In Table III, the yield ratio and the electron recapture probability of the fragmentation channels are shown.

Dissociation channels	Ratio (%)	Recapture probability (%)
Ar(1,1): 3.7 eV	47.39	
Ar(1,1): 5.2 eV	0.56	
Ar*(1,1): 7.2 eV	1.48	6.19
Ar(2,1): 7.4 eV	22.48	
Ar*(2,1): 14.2 eV	1.63	6.08
Ar*(2,1): 21.1 eV	0.005	-
Ar(1,2): 7.4 eV	1.01	
Ar*(1,2): 14.2 eV	0.28	1.06
Ar*(1,2): 21.1 eV	0.018	-
Ar(2,2): 14.4 eV	24.89	
Ar*(2,2): 21.8 eV	0.26	-

Table III. The yield ratio and electron recapture probability of the fragmentation channels of Ar_2 with intermediate intensity. The yield ratio is normalized to the total counts of the observed dissociation channels. The electron recapture probability is estimated by normalizing the yield of the electron recapture channel to the total yield of all the channels with the same initial charge state.

As can be seen in Table III, of argon dimers with an initial charge $Q = 3$, about 6% are involved in the frustrated tunneling ionization mechanism. For the channels Ar(2,1) and Ar(1,2) the one electron recapture probability of ∼6% and ∼1% was calculated, respectively. For the other FTI peaks, the recapture probabilities could not be calculated, as it was not possible to find out the yield of argon dimers with an initial charge $Q = 5$ which are involved in fragmentation processes.

5.3 Carrier Envelope Phase (CEP) Dependence of FTI

So far, it has been shown that the measurement of excited neutral fragments after strong field laser interaction can be explained in terms of electron recapture due to the Coulomb field of the fragments. This process called frustrated tunneling ionization is explained in the context of the electron rescattering model. Since rescattering processes of electrons in laser fields are CEP dependent, we expect also a CEP dependence for the frustrated tunneling ionization mechanism. The measured CEP dependence has an offset to the CEP of the laser pulse. This offset is calibrated by comparing the measured CEP dependence to the CEP dependence of the argon atoms.

CEP dependence on KER

In a first step, the CEP dependence of the different KER regions will be explored. In the Fig. 5.10 one can see three distinct structures at the three KER energy regions corresponding to the the three peak in the KER spectrum of the Ar^+-Ar^+ fragmentation channel Ar(1,1). As can be seen in Fig. 5.11. the KER at 3.6 eV corresponding to the Coulomb explosion shows some modulations over the CEP but no clear insights can be obtained from Fig. 5.12 for the FTI peak at 7.2 eV as it seems that the fragments are distributed quite chaotically in this plot. This is due to the limited statistics available. To circumvent this obstacle of low statistics one has to look at other quantities where it could be possible to see some modulation over the CEP despite the limited statistics.

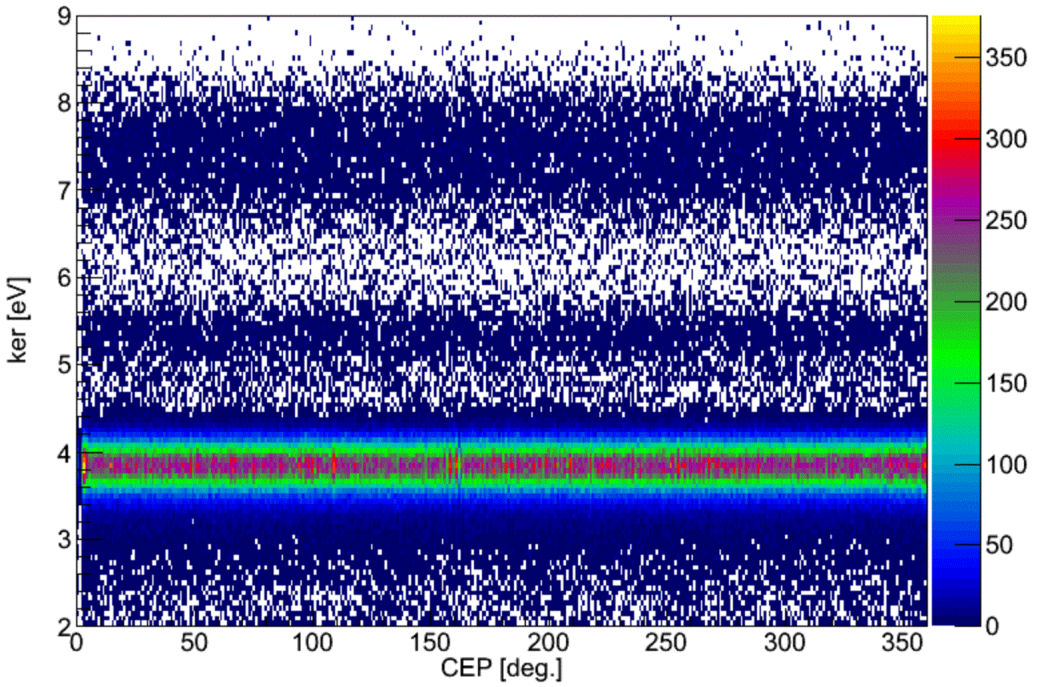

Fig. 5.10 KER spectrum plotted versus the CEP for the fragmentation channel Ar^+-Ar^+

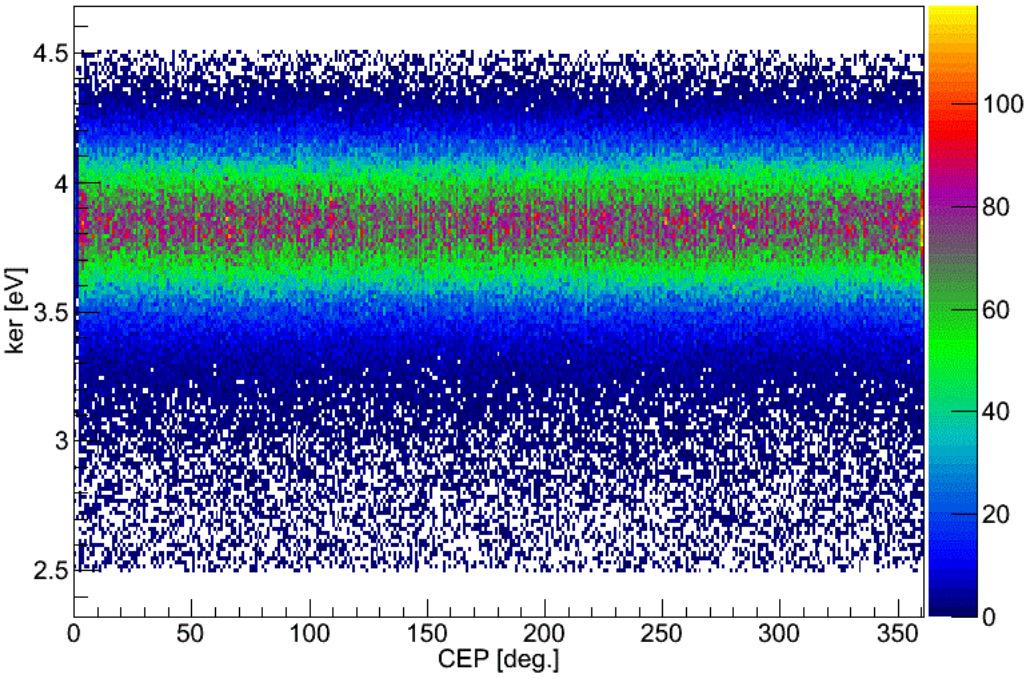

Fig. 5.11. KER spectrum plotted versus the CEP for selected KER range showing the Coulomb explosion peak

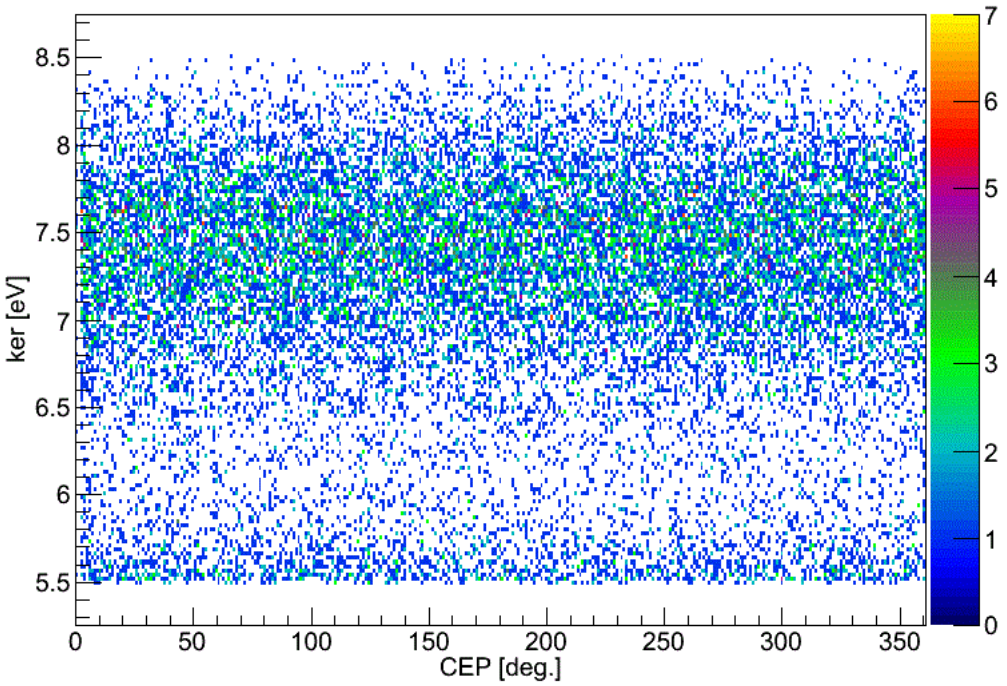

Fig. 5.12. KER spectrum plotted versus the CEP for selected KER range showing the FTI peak

CEP dependence of momentum sum (z-component)

One quantity which could resolve small modulations over the CEP is the sum momentum in the z-direction, the direction where we measure the coordinate with the time of flight, which can be measured with high precision. The measurement of the CEP dependence of the total momentum sum of the two argon ion fragments equals the total sum momentum of the ionized (and recaptured) electrons and is therefore interesting. The sum momentum must be close to zero if both particles are created as a result of a fragmentation process where the momentum is always conserved. The momentum of the electrons and photons can be neglected. Therefore, the momentum of the both particles must be equal and delivering a momentum sum close to zero.

$$p_{tot} = p^1_{ion} + p^2_{ion} + p_{electrons} + p_{photons} = 0 \tag{5.5}$$

$$\Rightarrow -p^1_{ion} \sim p^2_{ion} \tag{5.6}$$

In the following plots, the dependence of the momentum sum on the CEP will be discussed. To emphasize the modulation the integrated mean is calculated and plotted versus the CEP. Fig. 5.13 shows the CEP dependence of the singly ionized argon atoms.

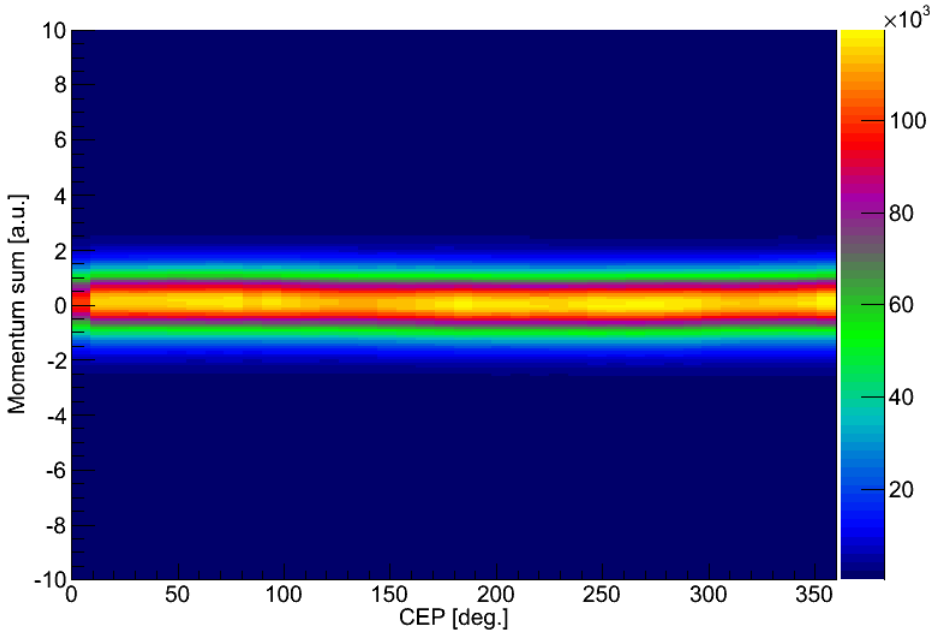

Fig. 5.13. Plot of the momentum sum versus CEP for argon atoms.

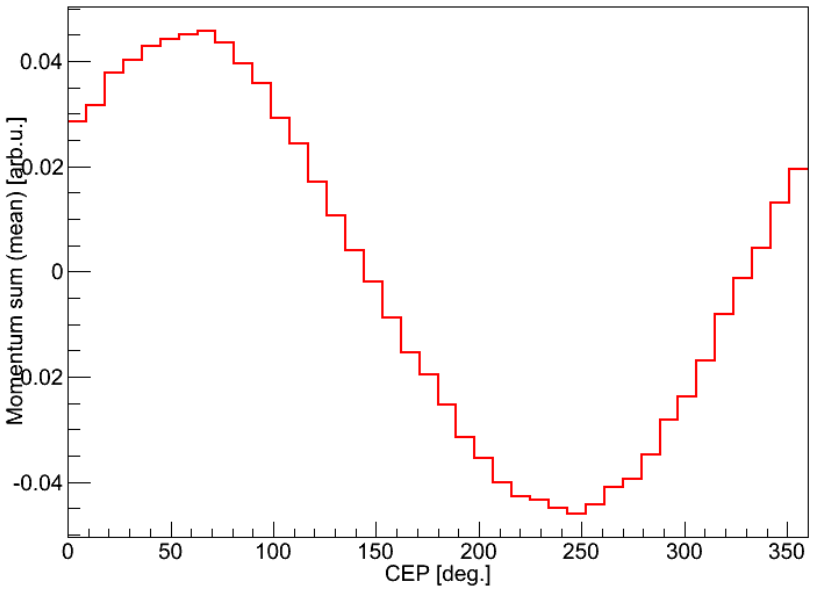

Fig. 5.14. Carrier envelope dependence of the singly-ionized argon atom.

Fig. 5.15 shows the CEP dependence of the doubly-ionized argon atoms. The doubly-ionized argon atoms have a qualitatively completely different CEP dependence than the singly-ionized argon atoms.

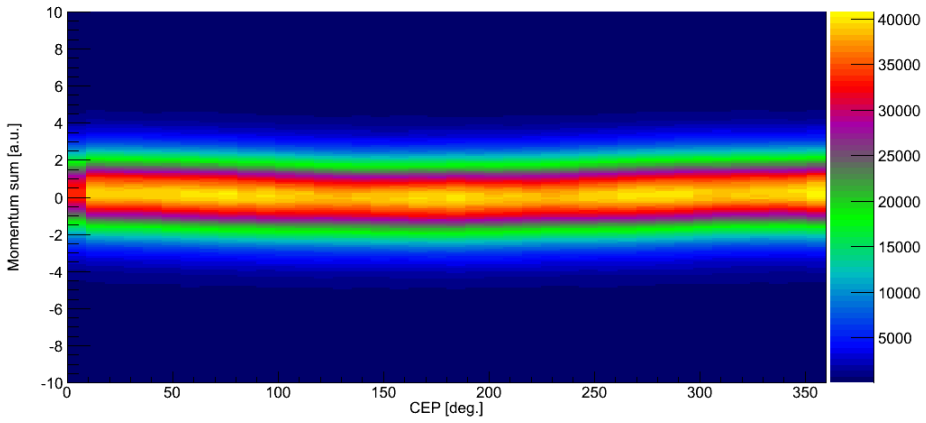

Fig. 5.15 Momentum sum versus CEP for doubly-ionized argon atoms.

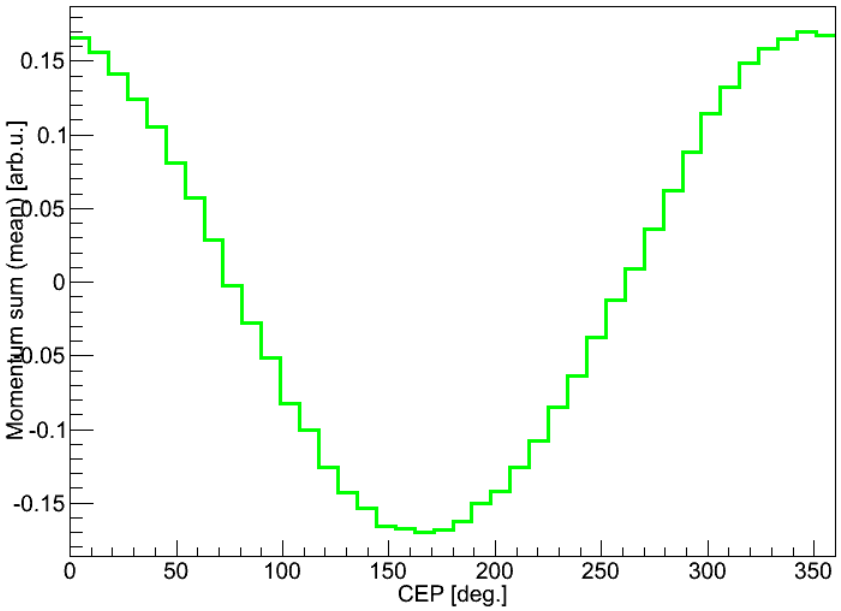

Fig. 5.16. Carrier envelope dependence of the doubly-ionized argon atom.

Fig. 5.17 shows the CEP dependence of the fragmentation channel Ar(1,1) where the doubly-ionized argon dimer fragments into two singly charged argon ions.

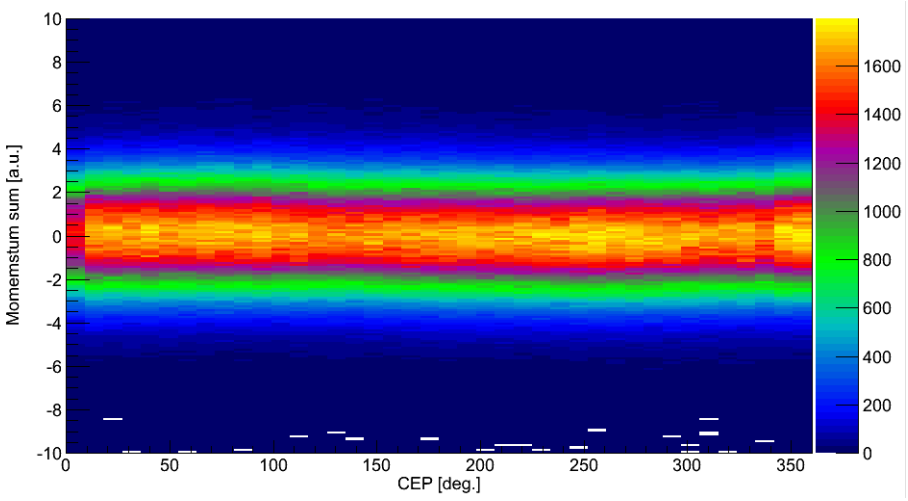

Fig. 5.17. Momentum sum versus CEP for the Ar^+-Ar^+ fragmentation channel.

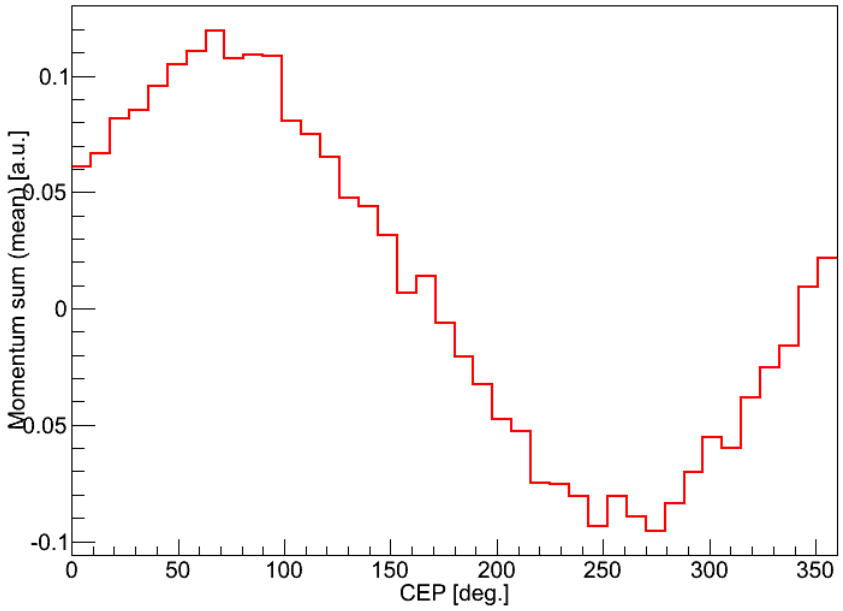

Fig. 5.18. Carrier envelope dependence of the Ar(1,1) fragmentation channel with the full KER range. Calculated mean of sum of the momentum component parallel to the laser polarization direction of the two fragments is plotted versus the carrier envelope phase.

Fig. 5.19 shows the CEP dependence of the coulomb explosion peak at 3.6 eV of the fragmentation channel Ar(1,1) where the doubly ionized argon dimer breaks into two singly charged argon ion fragments.

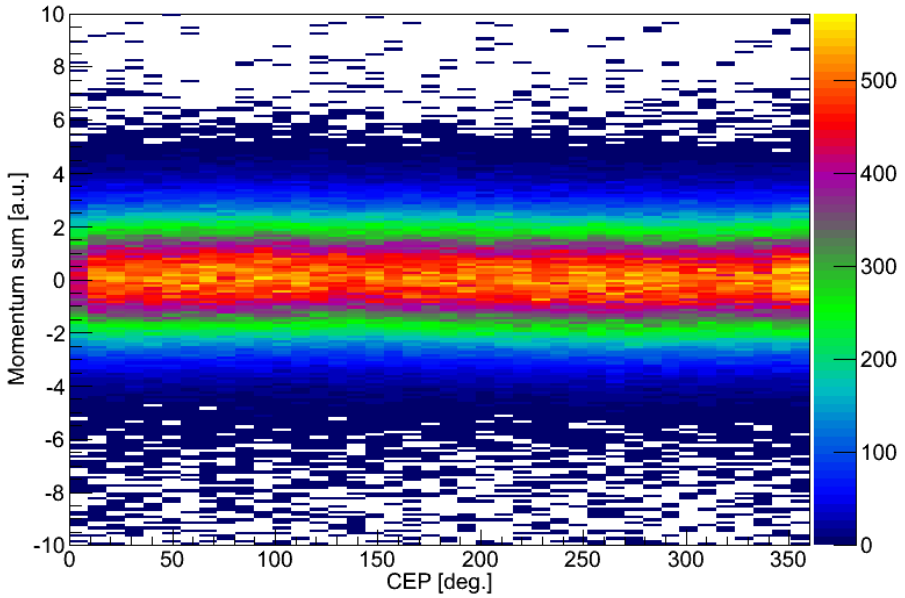

Fig. 5.19. Momentum sum versus CEP for the Coulomb explosion peak of the Ar^+-Ar^+ fragmen-

tation channel

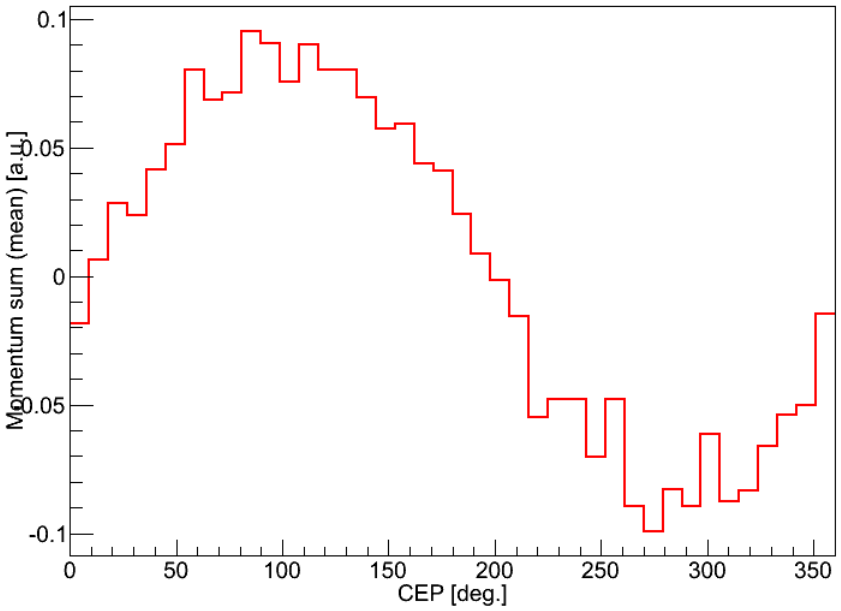

Fig. 5.20. Carrier envelope dependence of the Coulomb explosion peak of the Ar(1,1) fragmentation channel. Calculated mean of sum of the momentum component parallel to the laser polarization direction of the two fragments is plotted versus the carrier envelope phase.

As can be seen in Fig. 5.21, following dependence was found for the FTI peak of Ar(1,1) channel, the recapture of an electron by one singly charged argon ion. Due to low statistics no clear sinusoidal dependence is found, but 2π periodicity is visible.

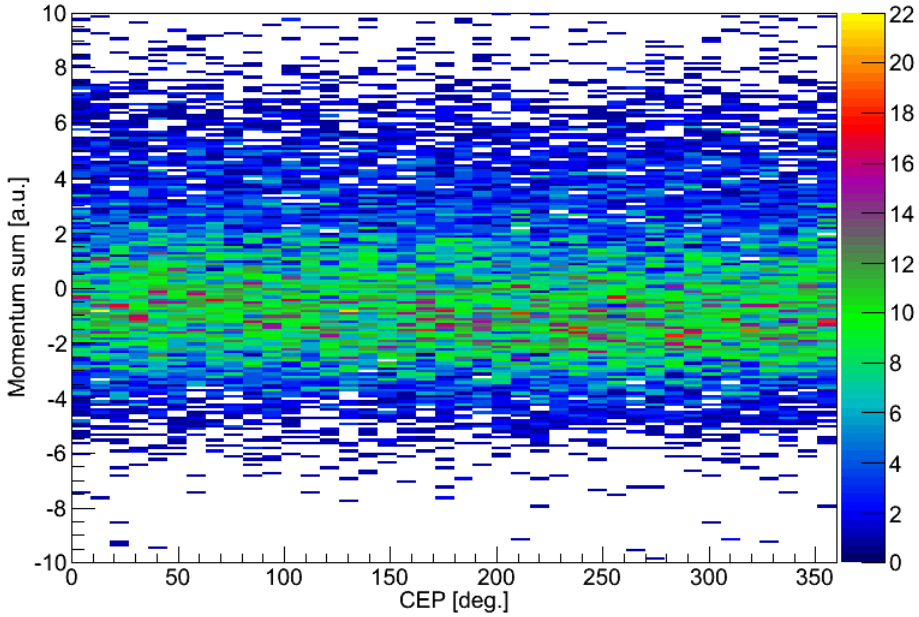

Fig. 5.21 Momentum sum versus CEP for the FTI peak of the Ar^+-Ar^+ fragmentation channel

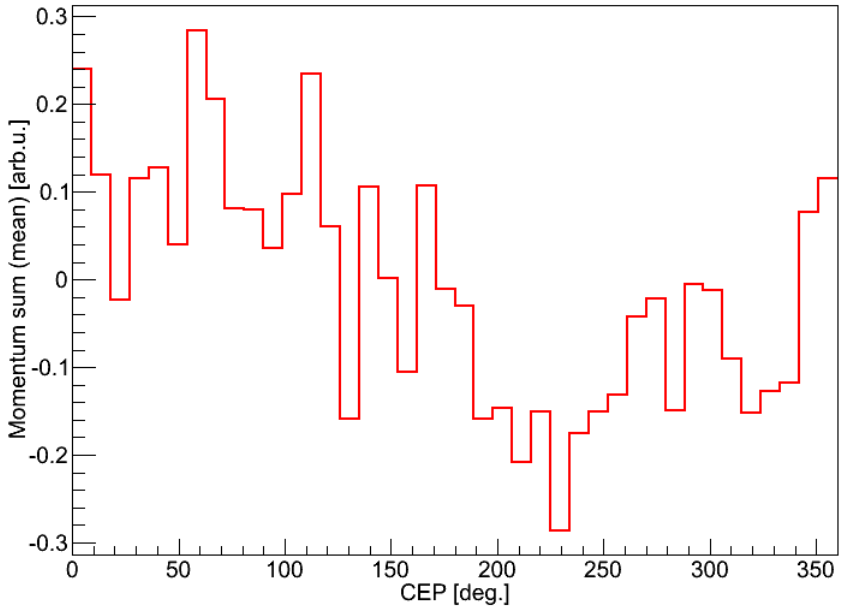

Fig. 5.22. Carrier envelope dependence of the frustrated tunneling ionization mechanism for Ar(1,1) fragmentation channel. Calculated mean of sum of the momentum component parallel to the laser polarization direction of the two fragments is plotted versus the carrier envelope phase.

Fig. 5.23 shows the CEP dependence of the fragmentation channel Ar(2,1) where the three fold ionized argon dimer fragments into a singly charged argon ion and a

doubly charged argon ion.

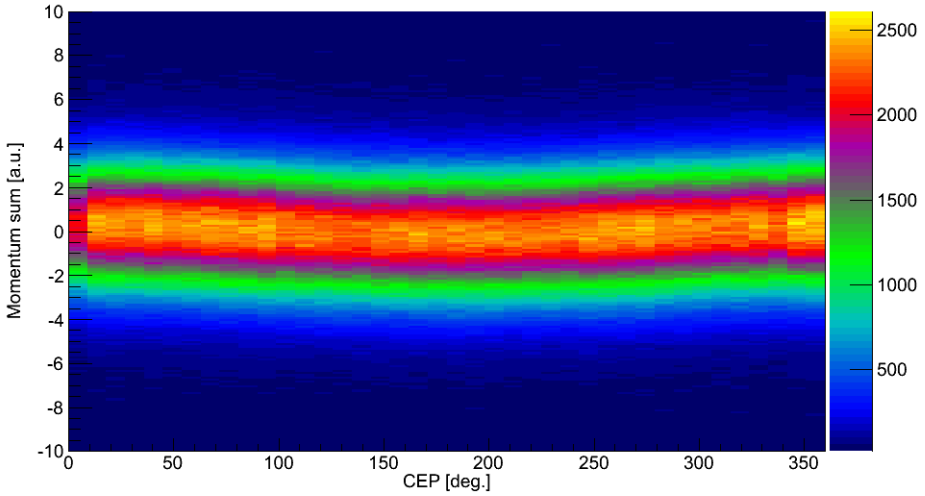

Fig. 5.23 Momentum sum versus CEP for the Ar^{2+}-Ar^{+} fragmentation channel

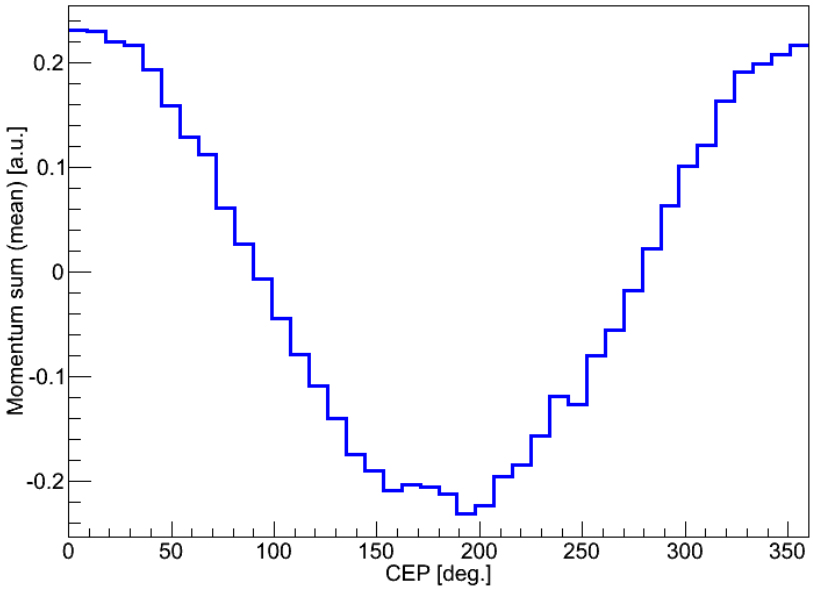

Fig. 5.24. Carrier envelope dependence of the Ar(2,1) fragmentation channel with the full KER range. Calculated mean of sum of the momentum component parallel to the laser polarization direction of the two fragments is plotted versus the carrier envelope phase.

Fig. 5.25 shows the CEP dependence of the Coulomb explosion peak of the fragmentation channel Ar(2,1) where the three fold ionized argon dimer fragments into a singly charged argon ion and a doubly charged argon ion.

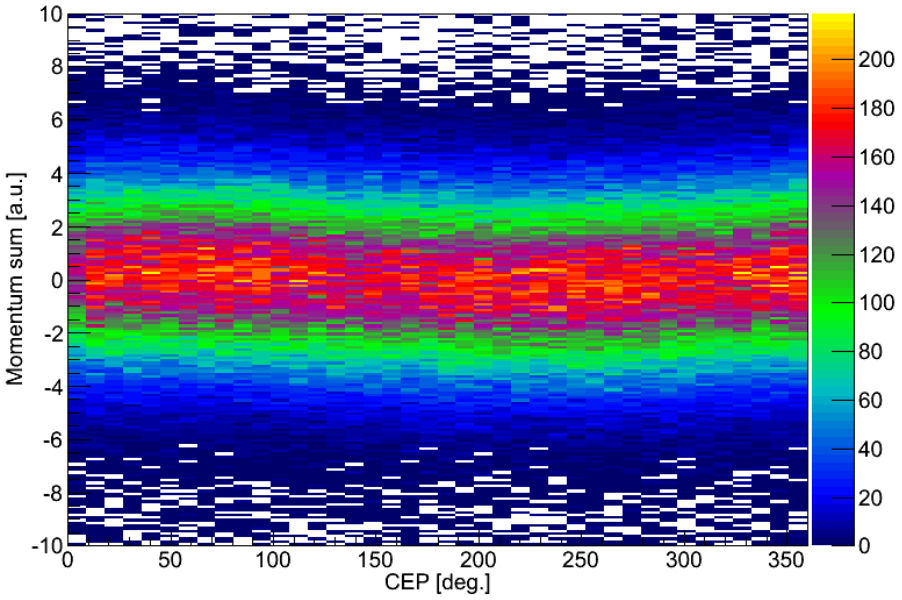

Fig. 5.26. Momentum sum versus CEP for the Coulomb explosion peak of the Ar^{2+}-Ar^{+} fragmentation channel

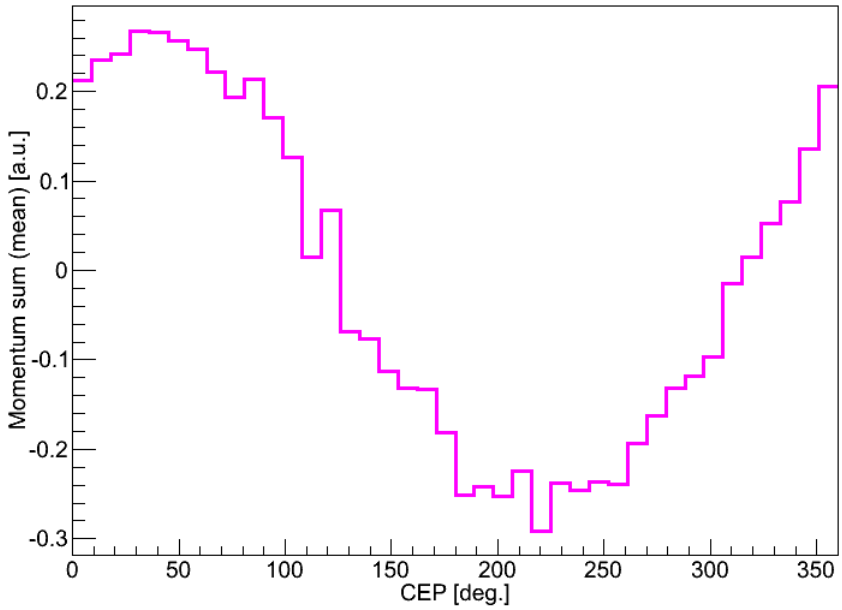

Fig. 5.27. Carrier envelope dependence of the Coulomb explosion peak of the Ar(2,1) fragmentation channel. Calculated mean of sum of the momentum component parallel to the laser polarization direction of the two fragments is plotted versus the carrier envelope phase.

As can be seen in Fig. 5.29, a more clear dependence was found for the FTI peak of the Ar(2,1) fragmentation channel. In this case from an initial Ar^{2+}-Ar^{2+} configuration,

one electron is recaptured by one of the two argon ions. Slightly more statistics (about 27500 counts) was available for this break up.

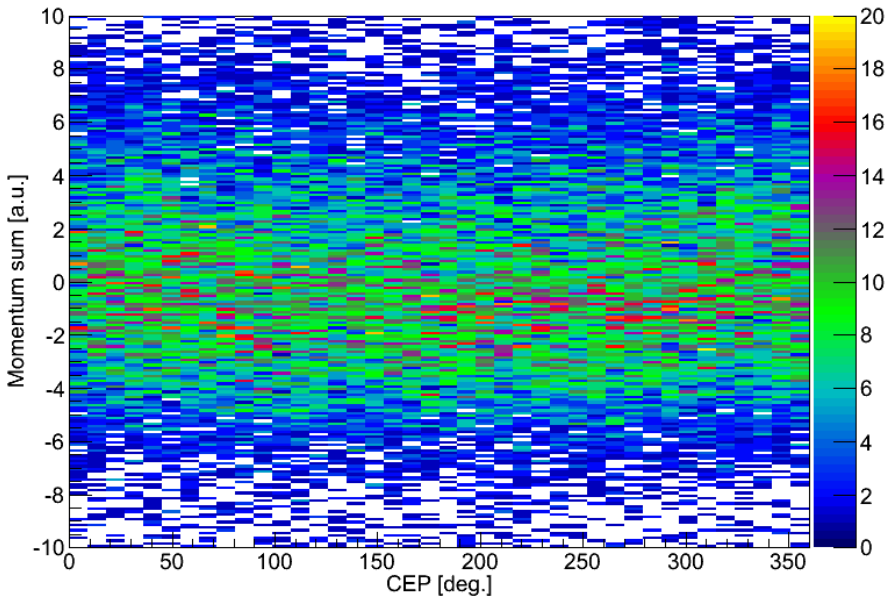

Fig. 5.28. Momentum sum versus CEP for the FTI peak of the Ar^{2+}-Ar^{+} fragmentation channel

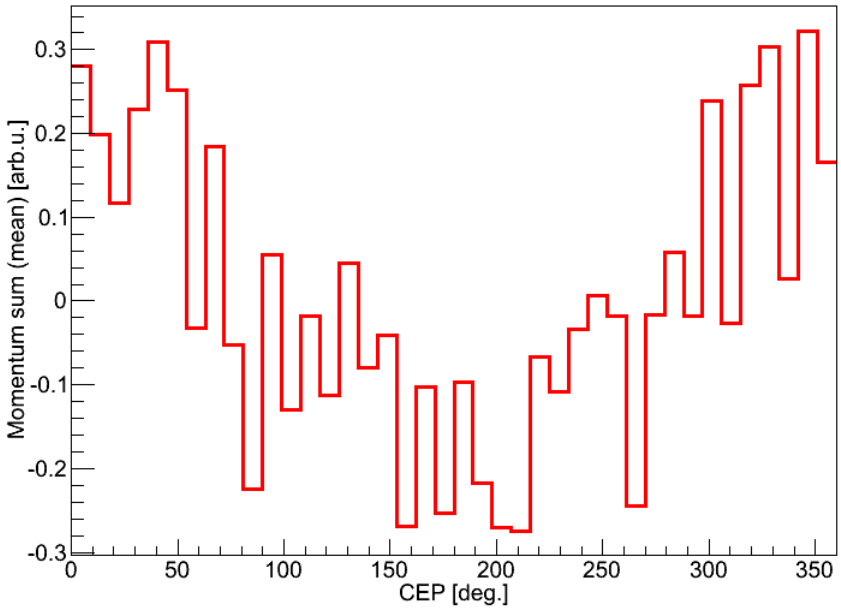

Fig. 5.29. Carrier envelope dependence of the frustrated tunneling ionization mechanism for the combined Ar(2,1) and Ar(1,2) fragmentation channels. Calculated mean of sum of the momentum

component parallel to the laser polarization direction of the two fragments is plotted versus the carrier envelope phase.

Next, we compare the measured CEP dependence of the frustrated tunneling ionization peaks to known signals. As the reference signals of the CEP dependence we take ionization of Ar atoms and of argon atoms and the standard Coulomb explosion signal of argon dimers, where no rescattering processes are involved. Electron rescattering processes can lead to small relative phase shifts in the CEP dependence of the electron sum momentum. However, the momentum transfer by the recaptured electron to the argon ion is very small which means that very precise measurements are needed to resolve the small phase shift.

As can be seen in Fig. 5.30 and Fig. 5.31, our results show a clearer CEP dependence for the Ar*(2,1) breakup than the Ar*(1,1). We propose that the charge asymmetry of the Ar*(2,1) breakup channel could be the reason why we see a more distinctive CEP dependence in this case. In the post-analysis we are able to distinguish between the two argon ions due to different charges which is not possible for the Ar*(1,1) breakup channel where both ions have the same charge. Another reason could be the higher yield we measured for the Ar*(2,1) channel in comparison to the Ar*(1,1) channel.

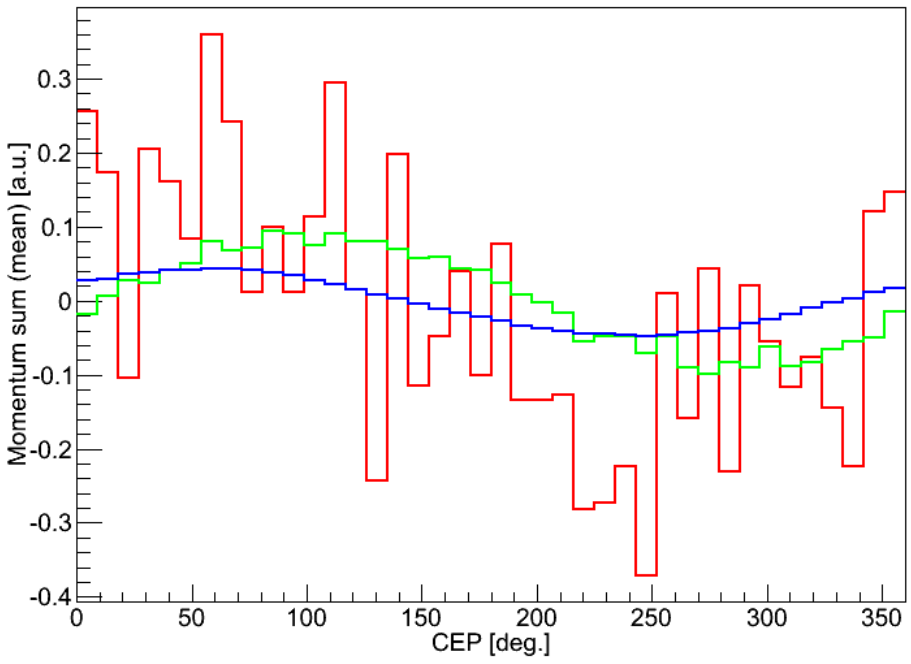

Fig. 5.30. Carrier envelope phase dependence of the argon atom ionization (blue line), argon dimer Coulomb explosion (green line) with the frustrated tunneling ionization mechanism (red line) for the Ar(1,1) fragmentation channel

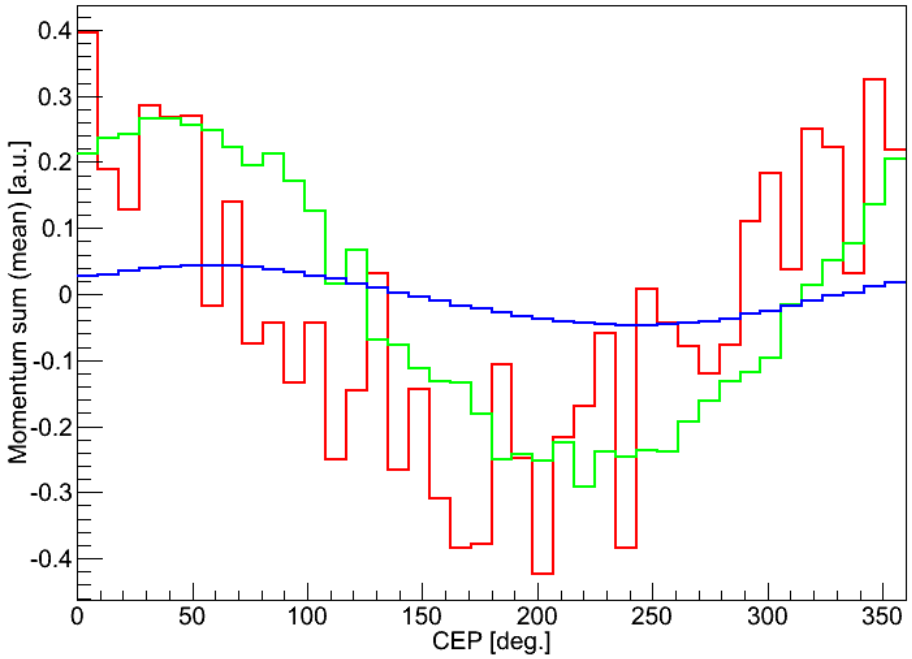

Fig. 5.31. Carrier envelope phase dependence of the argon atom ionization (blue line), argon dimer Coulomb explosion (green line) with the frustrated tunneling ionization mechanism (red line) for the Ar(2,1) fragmentation channel.

Calculated mean of sum of the momentum component parallel to the laser polarization direction of the two argon ion fragments is plotted versus the carrier envelope phase. In fact, as shown in Fig. 5.32, the CEP dependence of Ar*(2,1) peak almost resembles the CEP dependence of the Ar(2,2) Coulomb explosion peak which is no surprise since both KER peaks result from the same initially four times ionized argon dimer ion where in the case of Ar*(2,1), one electron gets recaptured. Nonetheless, there should be a very small relative phase shift in the CEP dependence of these two peaks due to the recapturing dynamics in one case.

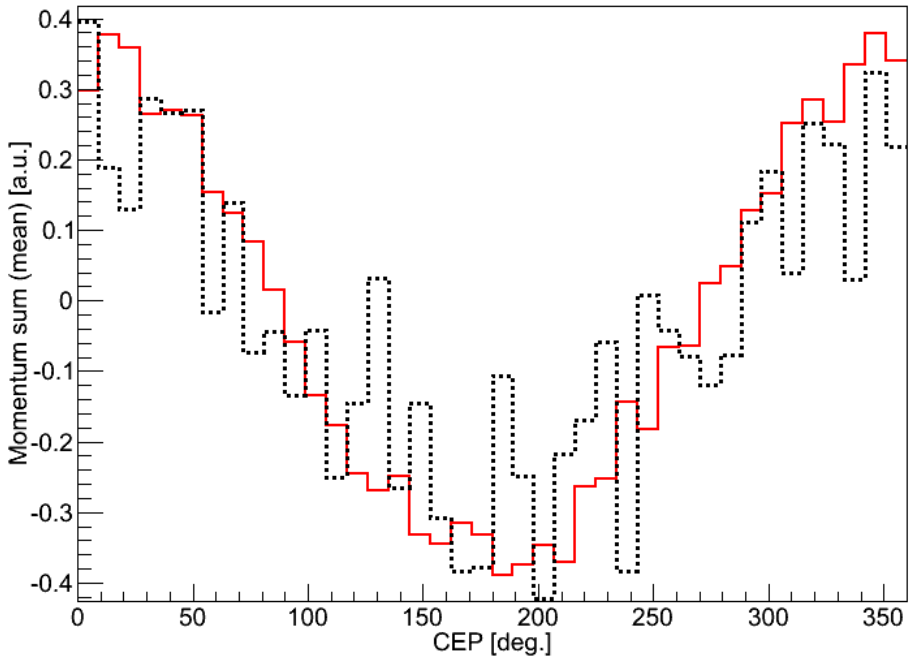

Fig. 5.32. Comparison of the carrier envelope phase dependence of the electron recapture peak denoted as Ar*(2,1) (black dotted line), with the Coulomb explosion (CE) peak (red line) of the Ar(2,2) fragmentation channel.

6 Conclusion and Outlook

In this work, ionization mechanisms of argon dimers subjected to intense laser fields were studied. Specifically, the focus was on the newly reported phenomenon termed frustrated tunneling ionization which is an electron recapture process. In this process, electrons which tunnel out of the atom due to external laser fields do not gain enough energy from the laser field to overcome the Coulomb field and become subsequently trapped into high lying Rydberg states. With pulses as short as 5 fs, strong field ionization processes proceed quite differently and reveal a variety of different behavior patterns. One example is above-threshold ionization spectra of photoelectron which shows a dependence on the carrier envelope phase of the pulse. Using a phasemeter which is based on this phenomenon, we verified the proposed rescattering nature of the FTI process by studying the carrier envelope phase dependence of the FTI process.

We report for the first time to our knowledge, an experimental observation of an FTI process for argon dimers with 5-fs laser pulses. We also observe, for the first time, a CEP dependence of this effect. Interestingly, in this work we measured a pronounced dependence was measured for the Ar^{2+}-Ar^{+} fragmentation channel, where after sequential double ionization of each argon atom, one of the two doubly charged argon ions recaptures a tunneled electron. For the FTI peak of the fragmentation channel Ar^{+}-Ar^{+} where after three fold sequential ionization of the argon dimer, one electron is recaptured by the higher charged argon ion, the CEP dependence was not very clear but an angular dependence of the different ker peaks was observed. It was shown that, those dimers which are oriented orthogonal to the laser polarization direction are more likely to be recaptured. Furthermore, it was noticed that the CEP dependence of the FTI peak corresponds to the Coulomb explosion peak of the dimer in absence of a recapturing process (for example the FTI peak Ar^{+*}-Ar^{+} corresponds to the Coulomb explosion peak of Ar^{2+}-Ar^{+}). Furthermore the results obtained with 5 fs laser pulses were compared with published results with longer pulse durations. The results indicate that recapturing processes play a proportionally similar role with short pulses as with

longer pulses which could not be expected beforehand. It is intuitively understandable that electron recapturing processes should exist in the case of excitation with multi-cycle pulses. The fact documented in our work that the recapture process also takes place few cycle 5 fs pulses is very interesting and opens up wide opportunities for further experimentation and refinements of the FTI theory.

A Appendix

A.1 Abbreviations

- ATI: Above Threshold Ionization
- CAD: Computer Aided Design
- CE: Coulomb Explosion
- CEO: Carrier Envelope Phase Offset
- CEP: Carrier Envelope Phase
- COLTRIMS: Cold Target Recoil Ion Momentum Spectroscopy
- CPA: Chirped Pulse Amplification
- DI: Double Ionization
- FTI: Frustrated Tunneling Ionization
- FWHM: Full Width Half Maximum
- GaN: Gallium Nitride
- KER: Kinetic Energy Release
- LES: Low Energy Structure
- LMF: List Mode File
- MCP: Micro Channel Plate
- Nd:YAG: Neodymium-doped Yttrium Aluminium Garnet
- Nd:YLF: Neodymium-doped Yttrium Lithium Fluoride
- Nd:YVO Neodymium-doped Yttrium Orthovanadate
- PIPICO: Photo-Ion Photo-Ion Coincidence
- RCT: Radiative Charge Transfer
- SFA: Strong Field Approximation
- Ti:sa: Titanium Sapphire
- VLES: Very Low Energy Structure
- ZES: Zero Energy Structure

A.2 List of Tables

A.3 List of Figures

a function of θ, the angle between the laser beam polarization axis and the direction of emission of one of the Ar^+ ions.

- Fig. 3.6. The KER spectrum of various fragmentation channels of Ar_2 after strong field ionization.
- Fig. 3.7. Kinetic energy release spectra of the fragmentation channels of N_2Ar (1,1), N_2Ar (1,2), N_2Ar (2,1), and N_2Ar (2,2).
- Fig. 3.8. Electron momentum distributions obtained by, measurement (top) and simulations (bottom) for argon after interacting with 68-fs laser pulses with a high peak intensity of $I_0 = 0.9 \times 10^{14}$ W/cm^2 is given with $p\perp$ on linear (left) and logarithmic (right) scales.
- Fig. 4.1. The 10 pass multipass amplifier consists of a 4-pass pre-amplifier and a 6-pass amplifier.
- Fig. 4.2. Dependence of the ultrashort laser pulse on its carrier envelope phase offset ϕ_0 where f_{rep} is the repetition rate and f_{ceo} the carrier envelope frequency.
- Fig. 4.3. CAD model of a single shot stereo ATI device (phasemeter).
- Fig. 4.4. Parametric asymmetry plot where A_{high} is plotted versus A_{low}.
- Fig. 4.5. Phase potato of the fragmentation channel Ar^+-Ar^+. The axis labels a1 and a2 stand for A_{high} and A_{low}.
- Fig. 4.6. Phase potato of the fragmentation channel Ar^+-Ar^+ with the KER selection of the coulomb explosion peak. The axis labels a1 and a2 stand for A_{high} and A_{low}.
- Fig. 4.7. Phase potato of the fragmentation channel Ar^+-Ar^+ with the KER selection of the second KER peak at 5.3 eV. The axis labels a1 and a2 stand for A_{high} and A_{low}.
- Fig. 4.8. Phase potato of the fragmentation channel Ar^+-Ar^+ with the KER selection of the frustrated tunneling ionization peak 7.2 eV. The axis labels a1 and a2 stand for A_{high} and A_{low}.
- Fig. 4.9. Schematic of the COLTRIMS setup modeled with CAD. The inlet shows the working setup.
- Fig. 4.10. Schematic of the supersonic gas expansion.
- Fig. 4.11. Photo of the COLTRIMS spectrometer.
- Fig. 4.12. Schematic of a micro-channel plate (MCP).
- Fig. 4.13. Image of an MCP and close up on the tubes under an electron microscope.
- Fig. 5.1. Time sum of the u-layer of the delay line anode with raw data. The plot shows that the time sum is not calibrated and takes nonzero values.
- Fig. 5.2. Time sum of the u-layer of the delay line anode with calibrated data. The plot shows that the time sum is calibrated as the time sum takes values close to zero.
- Fig. 5.3. Time of flight (ToF) spectrum. The sharp peaks can be unambiguously assigned to different fragments.

- Fig. 5.4. Photoion-Photoion coincidence (PIPICO) Plot. Time of flight on one fragment is plotted against the time of flight of the second fragment. The curved lines correspond to correlated two body events and the straight lines to atomic ionization processes.
- Fig. 5.5. Density plot of the magnitude of the vector momentum sum of the argon ions versus their KER for the Ar^+-Ar^+ dissociation channel Ar(1,1).
- Fig. 5.6. Density plot of the magnitude of the vector momentum sum of the argon ions versus their KER for the combined Ar^{2+}-Ar^+ and Ar^+-Ar^{2+} dissociation channels Ar(2,1) and Ar(1,2).
- Fig. 5.7. Density plot of the magnitude of the vector momentum sum of the argon ions versus their KER for the Ar^+-Ar^+ dissociation channel Ar(2,2).
- Fig. 5.8. Kinetic energy release (KER) spectra of the fragmentation channels (Eq. 5.1 to 5.4) with intermediate intensity with logarithmic scale. The black line shows the KER of channel Ar(1,1), the red line Ar(2,1) and the blue line Ar(2,2).
- Fig. 5.9. Yield of the particles with different KER selections depending on the orientation of the laser polarization direction. The laser polarization direction is parallel to the dimer orientation for $\cos(\theta) = 1$.
- Fig. 5.10 KER spectrum plotted versus the CEP for the fragmentation channel Ar^+-Ar^+.
- Fig. 5.11. KER spectrum plotted versus the CEP for selected KER range showing the CE peak.
- Fig. 5.12. KER spectrum plotted versus the CEP for selected KER range showing the FTI peak.
- Fig. 5.13. Plot of the momentum sum versus CEP for argon atoms.
- Fig. 5.14. Carrier envelope dependence of the singly ionized argon atom.
- Fig. 5.15 Momentum sum versus CEP for doubly ionized argon atoms.
- Fig. 5.16. Carrier envelope dependence of the doubly ionized argon atom.
- Fig. 5.17. Momentum sum versus CEP for the Ar^+-Ar^+ fragmentation channel.
- Fig. 5.18. Carrier envelope dependence of the Ar(1,1) fragmentation channel with the full KER range. Calculated mean of sum of the momentum component parallel to the laser polarization direction of the two fragments is plotted versus the carrier envelope phase.
- Fig. 5.19. Momentum sum versus CEP for the Coulomb explosion peak of the Ar^+-Ar^+ fragmentation channel.
- Fig. 5.20. Carrier envelope dependence of the Coulomb explosion peak of the Ar(1,1) fragmentation channel. Calculated mean of sum of the momentum component parallel to the laser polarization direction of the two fragments is plotted versus the carrier envelope phase.
- Fig. 5.21 Momentum sum versus CEP for the FTI peak of the Ar^+-Ar^+ fragmentation channel.
- Fig. 5.22. Carrier envelope dependence of the frustrated tunneling ionization mechanism for Ar(1,1) fragmentation channel. Calculated mean of sum of the momentum component parallel to the laser polarization direction of the two fragments is plotted versus the carrier envelope phase.

- Fig. 5.23 Momentum sum versus CEP for the Ar^{2+}-Ar^{+} fragmentation channel.
- Fig. 5.24. Carrier envelope dependence of the Ar(2,1) fragmentation channel with the full KER range. Calculated mean of sum of the momentum component parallel to the laser polarization direction of the two fragments is plotted versus the carrier envelope phase.
- Fig. 5.26. Momentum sum versus CEP for the Coulomb explosion peak of the Ar^{2+}-Ar^{+} fragmentation channel.
- Fig. 5.27. Carrier envelope dependence of the Coulomb explosion peak of the Ar(2,1) fragmentation channel. Calculated mean of sum of the momentum component parallel to the laser polarization direction of the two fragments is plotted versus the carrier envelope phase.
- Fig. 5.28. Momentum sum versus CEP for the FTI peak of the Ar^{2+}-Ar^{+} fragmentation channel.
- Fig. 5.29. Carrier envelope dependence of the frustrated tunneling ionization mechanism for the combined Ar(2,1) and Ar(1,2) fragmentation channels. Calculated mean of sum of the momentum component parallel to the laser polarization direction of the two fragments is plotted versus the carrier envelope phase.
- Fig. 5.30. Carrier envelope phase dependence of the argon atom ionization (blue line), argon dimer Coulomb explosion (green line) with the frustrated tunneling ionization mechanism (red line) for the Ar(1,1) fragmentation channel.
- Fig. 5.31. Carrier envelope phase dependence of the argon atom ionization (blue line), argon dimer Coulomb explosion (green line) with the frustrated tunneling ionization mechanism (red line) for the Ar(2,1) fragmentation channel.
- Fig. 5.32. Comparison of the carrier envelope phase dependence of the electron recapture peak denoted as Ar*(2,1) (black dotted line), with the Coulomb explosion (CE) peak (red line) of the Ar(2,2) fragmentation channel.

References

[1] T. Südmeyer, S.V. Marchese, Femtosecond laser oscillators for high field science, Nature photonics, Vol. 2, 599-604 (2008)

[2] F. Krausz, M. E. Fermann, Femtosecond solid-state lasers, IEEE Journal of Quantum Electronics, Vol. 28, 2097-2122 (1992)

[3] Ti:sapph laser. URL: http://en.wikipedia.org/wiki/Ti-sapphire_laser

[4] D.J. Kane, R. Trebino, Characterization of Arbitrary Femtosecond Pulses Using Frequency-Resolved Optical Gating, IEEE Journal of Quantum Electronics, Vol. 29, 571-579 (1993)

[5] C. Iaconis, I.A. Walmsley, Self-Referencing Spectral Interferometry for Measuring Ultrashort Optical Pulses, IEEE Journal of Quantum Electronics, Vol. 35, 501-509 (1999)

[6] P. Maine, D. Strickland, Generation of Ultrahigh Peak Pulses by Chirped Pulse Amplification, IEEE Journal of Quantum Electronics, Vol. 24, 398-403 (1988)

[7] T. Schultz and M. Vrakking: Attosecond and Free electron Laser Science, Chap. 1, 14:16, pages 1-4, 2012/4/5

[8] Strong-field ionization. URL: https://www.helmholtz-berlin.de/forschung/oe/fg/mi-synchrotron-radiation/synchrotron/photons/x-ray-pulses/high-harmonic-generation/index_en.html

[9] I. Shchatsinin. Free clusters and free molecules in strong, shaped laser field. PhD thesis, Freie Universität Berlin, 2009.

[10] T. Nubbemeyer et al., Strong-Field Tunneling without Ionization, Phys. Rev. Lett. 101, 233001 (2008).

[11] B. Manschwetus et al., Strong Laser Field Fragmentation of H2: Coulomb Explosion without Double Ionization, Phys. Rev. Lett. 102, 113002 (2009).

[12] B. Manschwetus et al., Mechanisms underlying strong-field double ionization of argon dimers, Phys. Rev. A 82, 013413 (2010).

[13] B. Ulrich et al., Double-ionization mechanisms of the argon dimer in intense laser fields, Phys. Rev. A 82, 013413 (2010).

[14] J. Wu et al., Multiple Recapture of Electrons in Multiple Ionization of the Argon Dimer by a Strong Laser Field, Phys. Rev. Lett. 107, 043003 (2011).

[15] X. Xie et al., Tunneling electron recaptured by an atomic ion or a molecular ion, Phys. Rev. A 88, 065401 (2013).

[16] B. Wolter et al., Formation of very-low-energy states crossing the ionization threshold of argon atoms in strong mid-infrared fields, Phys. Rev. A 90, 063424 (2014).

[17] H. K. Gill. Bestimmung der Konfiguration einfacher Moleküle mittels Coulomb Explosion Imaging. Master's Thesis, Johann Wolfgang Goethe-Universität Frankfurt am Main, (2015).

[18] S. Roither. Investigation of Strong Laser Field-Induced Fragmentation Dynamics of Hydrocarbon Molecules using Coincidence Momentum Imaging. PhD thesis, Technische Universität Wien, (2011).

[19] M. Kitzler, S. Nagele. Lecture Notes in Attosecond Physics, Technische Universität Wien, (2013).

[20] MCP. URL: http://www.dmphotonics.com/MCP_MCPImageIntensifiers/microchannel_plates.htm

[21] MCP. URL: http://www.tectra.de/MCP.htm

[22] M. Schöffler. Entwicklung und Aufbau eines Abbildungssystems zur Messung von Elektronen jenseits niedriger Energien. Master's Thesis, Johann Wolfgang Goethe-Universität Frankfurt am Main, (2002).

[23] A. Sayler et al. Precise, real-time, every-single-shot, carrier-envelope phase measurement of ultrashort laser pulses, Opt. Lett. 36, 1 (2011).

[24] Carrier envelope phase. URL: https://en.wikipedia.org/wiki/Carrier-envelope_phase

[25] G. G. Paulus et al. Absolute-phase phenomena in photoionization with few-cycle laser pulses, Nature 414, 182-184 (2001)

[26] M. Nisoli et al. Compression of high-energy laser pulses below 5 fs, Optics Letters, Vol. 22, No. 8, (1997)

[27] M. G. Schätzel, Mehrphotonen-Ionizationsprozesse mit intensiven Laserpulsen. PhD thesis, Ludwig-Maximillians-Universität, München, (2006).

[28] Delay Line Anode. URL: http://www.roentdek.com/products/detectors/

[29] R. Dörner et al. Cold target recoil ion momentum spectroscopy: a 'momentum microscope' to view atomic collision dynamics. Physics Reports, vol. 330, no. 2-3, pp. 95-192, (2000).

[30] D. R. Miller. "Free Jet Sources" in Atomic and Molecular Beam Methods, ed. G. Scoles, Oxford University Press, Oxford/New York, (1988).